

# Evaluation of uncertainty in determination of neutral axis and deformed shape of beam structures

FINAL REPORT  
January 2016

Submitted by:

Branko Glisic  
Associate Professor

Princeton University  
Princeton University E330 EQuad  
Princeton, NJ 08544

External Project Manager  
Nagnath (Nat) Kasbekar, P.E.  
Deputy State Transportation Engineer,  
Director, Bridge Engineering & Infrastructure Management  
NJDOT

In cooperation with  
Rutgers, The State University of New Jersey  
And  
New Jersey  
Department of Transportation  
And  
U.S. Department of Transportation  
Federal Highway Administration

## **Disclaimer Statement**

The contents of this report reflect the views of the authors, who are responsible for the facts and the accuracy of the information presented herein. This document is disseminated under the sponsorship of the Department of Transportation, University Transportation Centers Program, in the interest of information exchange. The U.S. Government assumes no liability for the contents or use thereof.

1. Report No. <b>CAIT-UTC-048</b>	2. Government Accession No.	3. Recipient's Catalog No.	
4. Title and Subtitle <b>Evaluation of uncertainty in determination of neutral axis and deformed shape of beam structures</b>		5. Report Date <b>December 2015</b>	
		6. Performing Organization Code <b>CAIT/Princeton University</b>	
7. Author(s) <b>Branko Glisic</b>		8. Performing Organization Report No. <b>CAIT-UTC-048</b>	
9. Performing Organization Name and Address <b>Princeton University Princeton University E330 EQuad, Princeton, NJ 08544</b>		10. Work Unit No.	
		11. Contract or Grant No. <b>DTRT12-G-UTC16</b>	
12. Sponsoring Agency Name and Address <b>Center for Advanced Infrastructure and Transportation Rutgers, The State University of New Jersey 100 Brett Road Piscataway, NJ 08854</b>		13. Type of Report and Period Covered <b>Final Report 01/01/2014 – 12/31/2015</b>	
		14. Sponsoring Agency Code	
15. Supplementary Notes <b>U.S. Department of Transportation/Research and Innovative Technology Administration 1200 New Jersey Avenue, SE Washington, DC 20590-0001</b>			
16. Abstract  <p>With aging infrastructure, it becomes crucial to make informed decisions about maintenance and preservation actions, as well as renewal of civil structures. Structural Health Monitoring (SHM) can be an important aid in this decision process, but in spite of its great potential, SHM is not applied in a widespread or generic manner, which is essentially due to the lack of reliable and affordable monitoring solutions. Consequently, there is a demand for monitoring methods that are not specific to individual structures, are reliable and robust on-site, and applicable to typical bridges.</p> <p>The overall objective of PI's research group is to research and develop universal SHM methods based on strain monitoring using series of parallel long-gauge fiber-optic sensors (so called parallel topologies). In particular, two basic parameters are studied in detail: 1) the location of the neutral axis based on dynamic strain measurements and a probabilistic data analysis, and 2) the deformed shape of individual girders based on static and dynamic strain measurements. Information about these parameters assessed at several locations of the bridge can then be used to assess global structural behavior and health condition. Changes in these parameters over time can indicate variation in structural behavior due to change in operational conditions or damage. However, setting the thresholds necessities thorough uncertainty analysis in determination of the above parameters.</p> <p>Thus, the objectives of this project are to explore, understand and quantify (deterministically or statistically) the uncertainties in determination of the position of neutral axis and the deformed shape, where the latter are determined based on series of parallel long-gauge sensors. To achieve this aim, numerical modelling, experimental analysis, and field validation on a real bridges were performed.</p>			
17. Key Words <b>Uncertainty analysis, Neutral axis, Deformed shape, Structural health monitoring, Long-gauge fiber-optic sensors, Strain monitoring</b>		18. Distribution Statement	
19. Security Classification (of this report) <b>Classified one year after submission</b>	20. Security Classification (of this page) <b>Unclassified</b>	21. No. of Pages <b>44</b>	22. Price

## **Acknowledgments**

Testing of the ANDERS slab has been realized with great help and collaboration of Professor Gucunski's research group at Rutgers University, in particular Seong-Hoon Kee and Matthew Klein as well as Jersey Precast Inc., in particular Ross Jamieson. Graduate students helped with installation of the sensors on test structure and testing; thanks to Hiba Abdel-Jaber, Yao Yao, Michael Roussel, and Kaitlyn Kliewer.

The project on the US202/NJ23 highway overpass in Wayne has been realized with the important support, great help and kind collaboration of several professionals and companies. We would like to thank SMARTEC SA, Switzerland; Drexel University, in particular Professor Emin Aktan, Professor Frank Moon, and graduate student Jeff Weidner; New Jersey Department of Transportation (NJDOT); Long-Term Bridge Performance (LTBP) Program of Federal Highway Administration; PB Americas, Inc., Lawrenceville, NJ, in particular Mr Michael S Morales, LTBP Site Coordinator; Rutgers University, in particular Professors Ali Maher and Nenad Gucunski; All IBS partners; and Kevin the lift operator. Yao Yao helped with the sensor installation and Joseph Vocaturo designed and created sensor mounting equipment.

Professor Maria Feng and her group from Columbia University provided laser-based displacement measurement of the middle point of the longest span of the southeast leg of the Streicker Bridge. Dr. Marco Domaneschi from Polytechnic of Milan, Italy, helped the creation of finite element model of the the US202/NJ23.

Dr. Dorotea Sigurdardottir and Ms. Xi Li were graduate students whose extraordinary education, intelligence, hard work, passion, perseverance, and ethics made this project possible.

<b>Table of Contents</b>	<b>Page</b>
DESCRIPTION OF THE PROBLEM	1
APPROACH	2
METHODOLOGY	2
FINDINGS	3
CONCLUSIONS	33
PUBLICATIONS RESULTING FROM THE PROJECT	34
RECOMMENDATIONS	35
REFERENCES	36

## List of Figures

Figure 1. Left: the small scale testing specimen; the photo shows beam in a cantilevered configuration, with load at the free end. Right: examples of beam configurations with main geometrical and mechanical properties.	4
Figure 2. Left: The cross-section of the large scale composite bridge specimen in factory. Right: The bridge specimen simply supported on permanent supports.	4
Figure 3. Left: The finite element model of the large scale composite bridge specimen. Right: Modelling of the long-gauge fiber-optic strain sensors connected to girder flanges.	5
Figure 4. Left: The US202/NJ23 overpass consisting of concrete slab supported on steel girders. Right: Detail of the sensor positioning at the top and the bottom.	6
Figure 5. Left: Side view of the 3D model. Right: Mesh details of the steel beams with stiffening transversal elements under the concrete slab.	6
Figure 6. Left: View to the Streicker Bridge. Right: Embedding sensors in the Streicker Bridge.	7
Figure 7. FEM of the Streicker Bridge.	7
Figure 8. Schematic representation of the FBG sensor used in the project.	9
Figure 9: Left: example of cross-section equipped with two sensors for evaluation of the location of the neutral axis; Right: strain diagram in cross-section due to bending; labeling: $\varepsilon_t$ and $\varepsilon_b$ elastic strain values at the top and bottom sensor, $h$ – distance between sensors, $y_0$ – location of the neutral axis; and $d$ – distance from top sensor to the bottom of the cross-section.	11
Figure 10: Schematic representation of the influence of the elastic strain magnitude to the uncertainty of evaluation of the location of the neutral axis.	12
Figure 11: Normalized uncertainty in neutral axis location as a function of $ \delta\varepsilon/\varepsilon_b $ (left) and $ \delta\varepsilon/\varepsilon_t $ (right) for different values of $c$ .	12
Figure 12: Schematic representation of a multi-girder bridge with a concrete slab showing biaxial bending due to transverse location of the load with respect to the observed cross-section.	14

Figure 13: Schematic representation of the error in measurements using a parallel topology with two sensors under bi-axial bending (to simplify the presentation, the case presented in the figure assumes no normal force).	14
Figure 14: $\delta y^S/\alpha_s$ as a function of the ratio $M_y/M_x$ for different ratios of $I_x/I_y$ .	15
Figure 15. Schematic representation of long-gauge sensor in an inhomogeneous material.	16
Figure 16. Deformed shape, rigid body movements, and vertical displacement.	18
Figure 17: Curvature distribution due to concentrated forces $F_1$ and $F_2$ , uniform load $q$ , and concentrated couple $M$ , on a beam equipped with parallel sensors at $n+1$ points.	18
Figure 18. The three most common curvature distributions – linear, constant slope, and “broken line” – and corresponding load cases.	19
Figure 19. The error terms for double integration by the rectangle rule and trapezoid rule.	20
Figure 20: Schematic representation of large scale specimen and locations of simulated damage.	21
Figure 21. Schematic representation of the cross-sectional parameters needed for evaluation of the location of the centroid (left); the contributions of various parameters to the uncertainty of the location of the centroid, $\delta y_{centroid}$ (right).	22
Figure 22. The centroid of the cross-section, $y_{centroid}$ , and the neutral axis location determined from measurements, $\mu_w$ , along with their associated uncertainties are compared with a Z-score hypothesis test.	22
Figure 23: Various events that introduced bending in the specimen.	23
Figure 24: Comparison between the location of neutral axis and the centroid.	23
Figure 25: View to truck on the large scale specimen in close-to-real conditions.	24
Figure 26: Results of Z-score tests - the probability that the centroid and the neutral axis location coincide for Girders A, F, and K.	25
Figure 27: Neutral axis position sensitivity analysis – crack size.	26
Figure 28: Neutral axis position sensitivity analysis – imperfect support condition.	27
Figure 29: Dispersion of neutral axis in healthy and damage sections.	27
Figure 30: Dispersion of neutral axis – large scale specimen.	28
Figure 31. Small scale specimen testing setup.	29

Figure 32. The curvature and deformed shape of the small scale specimen loaded in cantilevered-beam configuration.	29
Figure 33. The curvature and deformed shape of the small scale specimen loaded approximately at the middle of the span, simple-beam configuration.	30
Figure 34. The curvature and deformed shape of the small scale specimen loaded with concentrated force at various locations, or with combination of forces, simple-beam configuration.	30
Figure 35. The curvature and deformed shape of the small scale specimen loaded with combination of concentrated force and uniformly distributed force.	31
Figure 36: Evaluation of uncertainties in determination of location of the neutral axis at midspan of girder 5 of the US202/NJ23 overpass.	32
Figure 37: Evaluation of the location of the neutral axis and associated uncertainty.	32
Figure 38. Deformed shape of the southeast leg of Streicker Bridge as obtained from SHM and FEM.	33

### **List of Tables**

Table 1. Error terms for rectangle and trapezoid rule for typical curvature distributions.	20
Table 2: The probability that the centroid and neutral axis location are not. Bold numbers are lower than 10%, italicized numbers are between 10% and 20%.	24

## DESCRIPTION OF THE PROBLEM

The US civil infrastructure is aging and has been identified as an area of critical need. ASCE estimates that current deterioration trends can have disastrous consequences in terms of costs (\$520 billion by year 2040), and socioeconomic impact (loss of ~ 400,000 jobs nationwide) [1]. In 2009, approximately 25% of bridge fleet in the US was identified as structurally deficient or functionally obsolete [2].

Majority of them are typical bridges, consisting of a concrete deck supported by steel girders (stringers). It is evident that sustainable preservation of existing infrastructure represents a goal that is essential for future vitality of the US economy and the prosperity of the US society. With aging infrastructure, it becomes crucial to make informed decisions about maintenance and preservation actions, as well as renewal of civil structures. Structural Health Monitoring (SHM) can be an important aid in this decision process, but in spite of its great potential, SHM is not applied in a widespread or generic manner, which is essentially due to the lack of reliable and affordable monitoring solutions. Consequently, there is a demand for monitoring methods that are not specific to individual structures, are reliable and robust on-site, and applicable to typical bridges. Two monitoring parameters that enable creation of such methods are 1) the location of the neutral axis and 2) deformed shape, as these parameters are universally present in beam-like structures.

Hence, the overall objective is to research and develop universal SHM methods based on strain monitoring using series of parallel long-gauge fiber-optic sensors (so called parallel topologies). In particular, two basic parameters are studied in detail: 1) the location of the neutral axis based on dynamic strain measurements and a probabilistic data analysis, and 2) the deformed shape of individual girders based on static and dynamic strain measurements. Information about these parameters assessed at several locations of the bridge can then be used to assess global structural behavior and health condition. Changes in these parameters over time can indicate variation in structural behavior due to change in operational conditions or damage.

Determination of these two parameters was successfully researched in the frame of previous UTC award (see report CAIT-UTC-012 [3]); however, in order to complete the methods, it is necessary to transform the data describing the parameters into actionable information to the end user (owner or manager of the structure). Therefore, it is crucial to create robust data analysis algorithms for damage identification (i.e., detection, localization, quantification, and prediction of structural capacity) and structural identification (i.e., evaluation of performance in terms of serviceability), which are major challenges in SHM in general. The robustness of the above algorithms strongly depend on the uncertainties associated with methods, and their evaluation is crucial for an accurate interpretation of data.

Thus, the objectives of this project are to explore, understand and quantify (deterministically or statistically) the uncertainties in determination of the position of neutral axis and the deformed shape, where the latter are determined based on series of parallel long-gauge sensors. To achieve this aim, numerical modelling, experimental analysis, and field validation on a real bridges were performed.

## APPROACH

Several sources of uncertainties related to the determination of the position of the neutral axis were identified [3]: (i) uncertainty of measurement of the SHM system, (ii) the magnitude of the measured strain, (iii) number and position of sensors, (iv) bi-axial bending, (v) gauge length of sensors, (vi) the change in axial strain, (vii) the size of SHM data sets, (viii) dynamic effects, and (ix) the position of the load on multi-girder systems. Due to time constraints, the scope of the project is limited only to factors (i)-(v), while other factors will be studied in the future research. The evaluation of uncertainty in determination of the position of the neutral axis was performed within the scope of this research (a) by exploring analytical expressions for influences (i)-(v), (b) by comparison with statistically analyzed data from real structures (Streicker Bridge and US202/NJ23 overpass), (c) by comparison with FE simulations (Abaqus), (d) by testing and validation in laboratory on small scale specimen, and (e) by validation on large scale physical model and real structures. Overall uncertainty is determined using the propagation formulas [4-5].

The accuracy in determination of deformed shape depends on [3]: (i) uncertainty of measurement, (ii) the gauge length of the sensors, (iii) the number and position of the sensors, (iv) loading pattern, and (v) the double integration method. The methodology presented for the neutral axis research, i.e., the above methods (a)-(e), are also applied in the analysis of the uncertainties of the deformed shape.

## METHODOLOGY

The project was realized in the period of January 1st, 2014 to December 31st, 2015. The work plan consisted of four tasks: 1) Creation of numerical models, 2) Creation of algorithms for determination of uncertainty in neutral axis position, 3) Creation of algorithms for determination of deformed shape, 4) Laboratory testing, and 5) Field validation.

### Task 1) Numerical simulations:

Small scale specimen (~1.6-m long), large scale specimen (~10-m long) and real structures (US202/NJ23 overpass in Wayne, NJ and Streicker Bridge in Princeton, NJ) were used for research and validation purposes. These structures were presented in detail in the next section.

The aim of Task 1 was to generate numerical models of these structures for the purposes of comparison with measurements, structural identification, and damage detection. The small scale specimen is a simple structure and beam-theory was used to model its behavior. Numerical models of the large scale specimen and US202/NJ23 overpass and Streicker Bridge were created in Finite Element software package 'Abaqus'.

### Task 2) Creation of algorithms for determination of uncertainty in neutral axis position:

The aim of this task was to create algorithms for determination of uncertainty for the factors (i)-(v) described in previous section. Algorithms were tested by using and comparing the results obtained from both numerical simulations and tests. Final validation was performed using data from US202/NJ23 overpass.

Iterative improvement of numerical models created in Task 1) was made through this task based on test results and results from field (US202/NJ23 overpass).

Task 3) Creation of algorithms for determination of uncertainty in deformed shape:

The aim of this task was to create algorithms for determination of uncertainty for the factors (i)-(v) described in previous section. Algorithms were tested by using and comparing the results obtained from both numerical simulations and tests. Final validation was performed using data from Streicker Bridge.

Iterative improvement of numerical models created in Task 1) was made through this task based on test results and results from field (Streicker Bridge).

Task 4) Laboratory testing:

The aim of this task was to create data-sets for calibration of numerical models presented in Task 1 and testing the algorithms created in Tasks 2 and 3.

Small scale testing specimen was completely built along with testing frame (see description in the next section); fiber optic sensors and LVDT displacement meters were installed and several types of test performed including: free vibration, forced vibration, incremental static, quasi-static, and dynamic load test; frame enabled change in structural system of the specimen, so cantilever and simply supported beam configurations were tested.

Large scale specimen was already equipped with monitoring system in the frame of an earlier research and data collected under static and dynamic load. That data is used in innovative manner in this project, with the purposes as described above.

Task 5) Field monitoring:

Two structures were used in field validation of the algorithms, US202/NJ23 overpass and Streicker Bridge.

Monitoring of the US202/NJ23 overpass consisted of approximately eight measurement sessions per year, performed during the project; data collected in the past were also available for the project purposes. One session contained ten 'events', and each 'event' consisted of collecting data from long-gauge fiber optic strain sensors during passage of a heavy vehicle over the overpass.

Monitoring of the Streicker Bridge was continuous, with interruptions when the reading unit was needed in the lab or to perform monitoring sessions at US202/NJ23 overpass and Streicker Bridge. Data collected in the past were also available for the project purposes.

The measurements from both structures were used to calibrate and improve the numerical models developed in Task 1. Algorithms developed in Tasks 2 and 3 were implemented and validated. Feedback was used to improve and fine tune the algorithms.

## **FINDINGS**

### **Numerical modelling**

In order to use small scale specimen (~1.6-m long), large scale specimen (~10-m long) and real structures (US202/NJ23 overpass in Wayne, NJ and Streicker Bridge in Princeton, NJ) for research and validation purposes, their numerical models had to be developed first. Brief description of numerical models is presented as follows.

### Small scale specimen

Small scale testing specimen was designed and constructed for laboratory validation purposes, see Figure 1. The specimen was 9.5-mm thick, and 254-mm wide aluminum plate, with length of 1.6 m. The frame for the specimen was designed and constructed, Fiber Bragg-Grating (FBG) long-gauge strain sensors and LVDT displacement-sensors were installed and calibrated. Furthermore, structural identification was performed through controlled static test, and as a result Young's modulus and moment of inertia were determined. The test frame allows for change in configuration, i.e., the following structural systems were created and tested: (1) cantilevered beam, (2) simply supported beam, and (3) beam with a roller on one side and fixed end at the other end. Small scale specimen was modelled using elementary equations of linear theory of structures (see Figure 1).

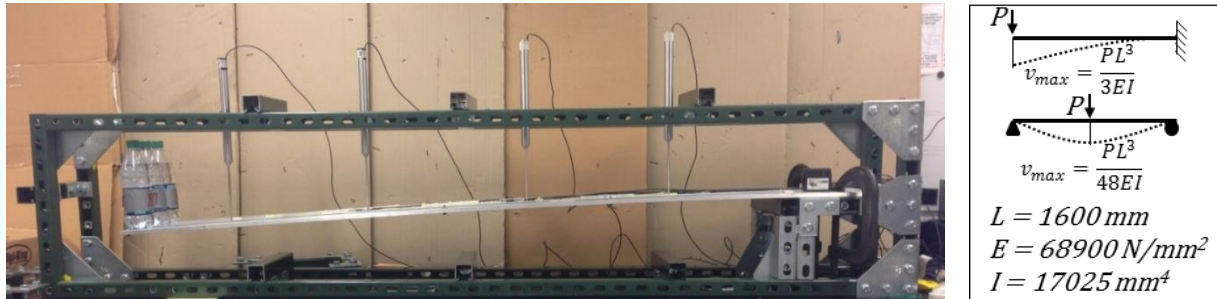


Figure 1. Left: the small scale testing specimen; the photo shows beam in a cantilevered configuration, with load at the free end. Right: examples of beam configurations with main geometrical and mechanical properties [8].

The small scale specimen was primarily used in evaluation of uncertainty of deformed shape as determined from series of parallel sensors.

### Large scale specimen

A large scale composite concrete-steel model bridge specimen was created as part of the Automated Nondestructive Evaluation & Rehabilitation System (ANDERS) Program at Rutgers University. The specimen consists of a 9-m by 3.6-m reinforced concrete deck at 2% grade, supported by three W16x57 steel I girders. Artificial minute damage was inserted into the slab by placing plastic sheets at locations of interest in advance of the casting of the concrete deck. The monitoring system included three sets of four parallel long-gauge fiber optic strain sensors and matching temperature sensors at two locations of minute damage, and one healthy reference location. The large scale specimen was monitored through a series of static and dynamic loading events. The cross-section of the specimen during lifting and the final arrangement of the structure simply-supported on permanent supports are shown in Figure 2.



Figure 2. Left: The cross-section of the large scale composite bridge specimen in factory. Right: The bridge specimen simply supported on permanent supports [8].

FEM software Abaqus was used to construct a finite element model for the large scale bridge specimen. Solid elements were used to simulate the concrete slab and the steel I girders. The model incorporated 12 steel C-shaped diaphragms connected to the three steel I girders, as well as longitudinal and transverse rebar embedded into the concrete slab. Fiber-optic strain sensors were simulated as truss elements and inserted inside the concrete slab or connected to the flanges of the steel I girders at locations of interest. The final mesh contains 155,647 nodes and 122,264 elements. The material properties used in the FEM model include the following: steel members with Young's modulus of 203 GPa, Poisson's ratio of 0.3; concrete members with Young's modulus of 34 GPa, Poisson's ratio of 0.2. Finite element analysis was used to predict the healthy location of the neutral axis, and to simulate behavior of the structure in the presence of minute damage. Figure 3 shows the cross-section of the structure in FEM and the FBG sensors attached to the steel I girder.

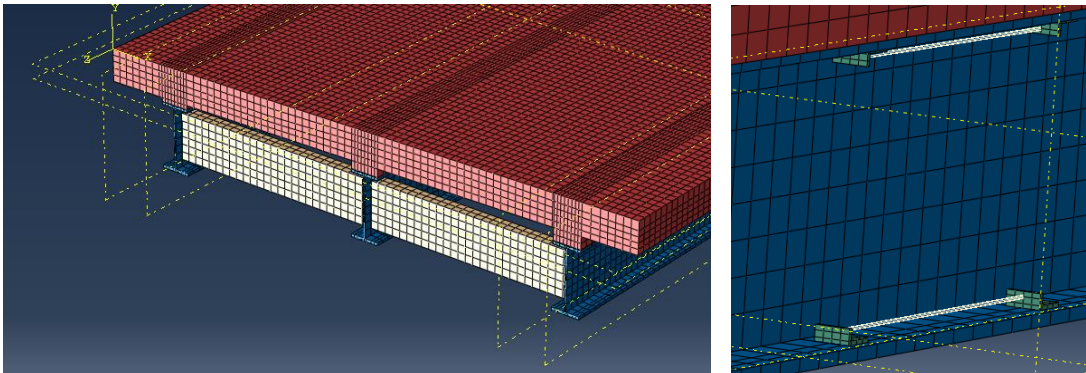


Figure 3. Left: The finite element model of the large scale composite bridge specimen. Right: Modelling of the long-gauge fiber-optic strain sensors connected to girder flanges [9].

The large scale specimen was primarily used in the evaluation of uncertainty of neutral axis position under various loading events.

#### US202/NJ23 Overpass, Wayne, NJ

US202/NJ23 Overpass close to Wayne, NJ, is typical composite concrete-steel structure built in 1980's. The Span 2 of the US202/NJ23 overpass consists of a skewed concrete slab (~18 m x 35 m) supported on eight stringers. The span is simply supported at both ends. Girders No. 2 and No. 5 were equipped with three sets of parallel long-gauge FBG strain sensors each (total of 12 sensors), in frame of International Bridge Study project. The approximate locations of sensors are in the middles and quarters of corresponding girders as shown in Figure 4.

The Finite Element Model (FEM) of the bridge was made using software Abaqus. This bridge was topic of the previous project [3], and description of numerical model as well as additional details regarding the bridge can be found in that report. The FEM consists of 55230 shell elements and 55556 nodes. The finite element mesh has been prepared within the Marc MSC code due to the effectiveness of its preprocessor for managing the mesh details and connections between longitudinal, transversal, vertical, and horizontal components of the structure. Subsequently the mesh was exported to software Abaqus. System identification was performed using free vibration (dynamic loading) of the structure, and the following mechanical

parameters are determined: Young modulus of 210 GPa and Poisson's ratio 0.3 for steel, and Young modulus of 30 GPa for the concrete slab, 35 GPa for the concrete piers and Poisson's ratio of 0.2 for both. Details of the FEM are given in Figure 5.



Figure 4. Left: The US202/NJ23 overpass consisting of concrete slab supported on steel girders. Right: Detail of the sensor positioning at the top and the bottom [6].

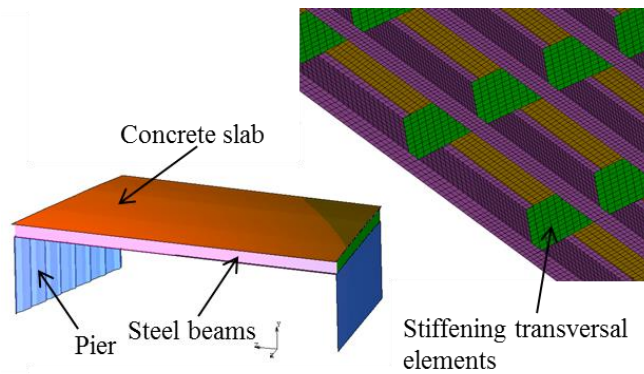


Figure 5. Left: Side view of the 3D model. Right: Mesh details of the steel beams with stiffening transversal elements under the concrete slab [7].

US202/NJ203 Overpass was mostly used for evaluation of uncertainties of the neutral axis.

### Streicker Bridge

Streicker Bridge is a pedestrian bridge built at Princeton University campus in 2009, and was open for traffic in 2010. Structurally, it consists of five parts: the main span and four approaching structures called legs. The main span is a deck-stiffened arch with span of 25 m and variable deck size, while the legs are curved continuous girders approximately 40-m long, with constant cross-section. In all bridge components, the deck consists of prestressed high-performance concrete deck, while the arch and the columns are built of weathering steel. A view to the structure is given in Figure 6. During the construction, series of FBG long-gauge strain sensors were embedded in a half of the main span and along entire south-east leg. View to sensors during the installation is given in Figure 6.



Figure 6. Left: View to the Streicker Bridge. Right: Embedding sensors in the Streicker Bridge.

A simple FEM was created for southeast leg in the software SAP2000 using frame elements. The boundary conditions and geometrical properties of the model are shown in Figure 7. The system identification was performed based on the test of the bridge, and the Young's modulus was estimated to be 35.4 GPa.

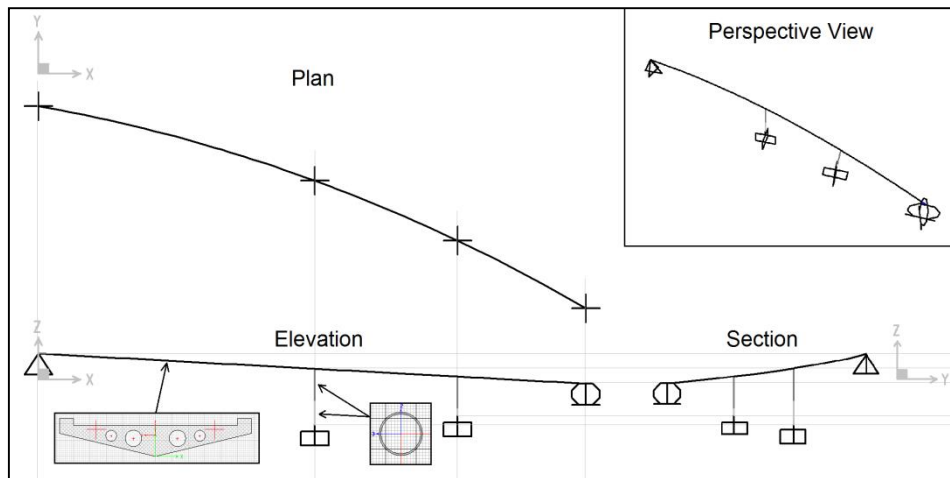


Figure 7. FEM of the Streicker Bridge [10].

The model presented above was modified in frame of the project in order to be expanded to entire bridge. However, due to high stiffness of the deck-stiffened arch, and subsequent small strains, the former was excluded from analysis, and only the southeast leg was studied in this project.

Streicker Bridge was used for evaluation of uncertainties of both the neutral axis and deformed shape.

### Creation of algorithms for determination of uncertainty in neutral axis position

The following sources of uncertainty in determination of neutral axis are identified [3]:

- (i) Uncertainty of measurement of the SHM system,
- (ii) The magnitude of the measured strain,

- (iii) Number and position of sensors,
- (iv) Bi-axial bending,
- (v) Gauge length of sensors,
- (vi) The change in axial strain,
- (vii) The size of SHM data sets,
- (viii) Dynamic effects, and
- (ix) The position of the load on multi-girder systems.

The algorithm for influences (i)-(v) are presented in this subsection. Other influences will be studied in the future research.

### Error and Uncertainty propagation

Error of measurement  $\delta y$  is difference between measured value and true value of measurand, as shown in Equation 1. Relative error  $\delta^* y$  is ratio between absolute error and true value of measurand, as shown in Equation 2.

$$\delta y = y_{measured} - y_{true} \quad (1)$$

$$\delta^* y = (y_{measured} - y_{true}) / y_{true} = \delta y / y_{true} \quad (2)$$

Error is, by its definition, a deterministic notion. When analyzing the measurements it is frequently of interest to assess minimum (maximum negative) and maximum (maximum positive) error. These values are called Limits of Errors.

Uncertainty of measurement  $u(A)$  is defined based on a confidence probability that error does not exceed some specified value. Standard uncertainty is defined as a standard deviation of the measurement error (probability of  $\delta A < u(A)$  is approximately 68%). Uncertainty is, by its definition statistical / probabilistic notion.

If the magnitude of observed parameter  $y$  is determined indirectly, as a function of several other directly monitored parameters  $x_1, x_2, \dots, x_n$ , i.e.,  $y=y(x_1, x_2, \dots, x_n)$  (e.g., elastic strain in steel structure is difference between total strain and thermal strain), then the error in estimation of magnitude of observed parameter can be determined using the propagation formulas:

$$\delta y = \frac{\partial y}{\partial x_1} \delta x_1 + \frac{\partial y}{\partial x_2} \delta x_2 + \dots + \frac{\partial y}{\partial x_n} \delta x_n \quad (3)$$

$$(u(y))^2 = \left( \frac{\partial y}{\partial x_1} u(x_1) \right)^2 + \left( \frac{\partial y}{\partial x_2} u(x_2) \right)^2 + \dots + \left( \frac{\partial y}{\partial x_n} u(x_n) \right)^2 \quad (4)$$

### (i) Uncertainty (error) of measurement of the SHM system

There are three main sources of the uncertainty of an SHM system: (a) random uncertainty (or random error), (b) systematic uncertainty (or systematic error), and (c) drift (loss of stability of the SHM system).

Random uncertainty can be determined by statistical tests, and its value is frequently provided by the manufacturer of the SHM system in terms of repeatability precision (standard deviation of repeated measurements under non-variable conditions of measurement) and reproducibility precision (standard deviation of repeated measurements under variable conditions of measurement).

Systematic uncertainty is usually not provided by the manufacturer, but could be determined by comparison with a calibrated measurement system. The two typical forms of occurrence of the systematic uncertainty are (a) offset / bias in measurement (the measurement is off from true value of measurand for a constant value) and (b) offset / bias in calibration constants (the calibration constants that transforms the encoding parameter into the measurand and are off by a constant value; for example, in the case of linear relation between the encoding parameter and the measurand the systematic uncertainty will be proportional to the magnitude of the measurand).

Drift represents a of measurement stability. It can be is mostly due to the nature of the SHM system, the ageing of components of the SHM system, and manufacturing errors. If it occurs slowly, in long term, it may be difficult to detect it and to quantify it.

While the value of the random uncertainty (or error) of an SHM system is frequently provided by the manufacturer of the SHM system, the values of systematic uncertainty (or error) and the drift of are usually not provided by the manufacturer and they should be evaluated by an independent calibration. However, previous research [3] demonstrated that static, long-term measurements, cannot be effectively used for the purposes of evaluation of location of the neutral axis, and that rather short-time dynamic measurements (e.g., due to passage of a very heavy vehicle), or very short-term static measurements (e.g., during the test of the bridge) should be used. In this way, the uncertainties related to systematic bias in measurement and drift can be practically eliminated, and the only potential bias in calibration constants should be further evaluated.

Additional source of uncertainty of an SHM system is influence of temperature variations to both the sensor and the monitored structure. In the specific case of sensors used in this research, i.e. the FBG sensors, the encoding parameter is back-reflected wavelength of the light, and each strain sensor is equipped with two FBG sensing elements, the first sensitive to both strain and temperature, and the other sensitive to temperature only. The sensor appearance is shown in Figure 8.

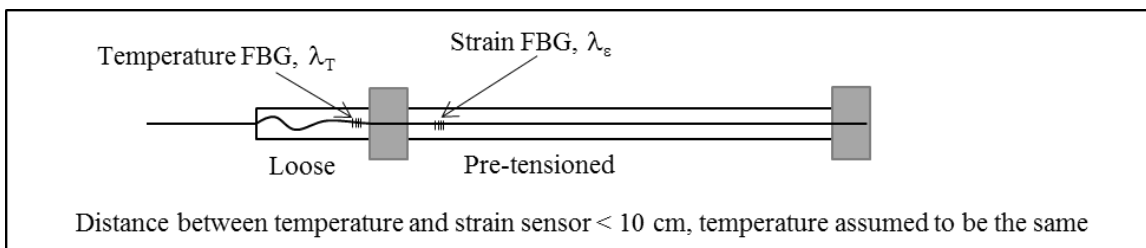


Figure 8. Schematic representation of the FBG sensor used in the project [6].

The relationship between the strain, temperature, and wavelengths of FBGs, as measured by SHM system are given in Equations 5 and 6.

$$\Delta T = \frac{1}{C_T} \Delta \lambda_T \quad (5)$$

$$\Delta \varepsilon_{tot} = \frac{1}{C_\varepsilon} \left( \Delta \lambda_\varepsilon - \frac{C_{T,\varepsilon}}{C_T} \Delta \lambda_T \right) \quad (6)$$

where the symbols in the equations are the following:

Symbol	Description
$\Delta \lambda_\varepsilon$	Change in wavelength measured by strain FBG [nm] (due to combined change of strain and temperature)
$\Delta \lambda_T$	Change in wavelength measured by temperature FBG [nm] (due to change of temperature)
$\Delta \varepsilon_{tot}$	Change in total strain [ $\mu\varepsilon$ ]
$\Delta T$	Change in temperature [ $^\circ\text{C}$ ]
$C_\varepsilon$	Strain calibration constant for strain FBG, typical value 0.0012 nm/ $\mu\varepsilon$
$C_{T,\varepsilon}$	Temperature calibration constant for strain FBG, typical value 0.01 nm/ $^\circ\text{C}$
$C_T$	Temperature calibration constant for temperature FBG, typical value 0.01 nm/ $^\circ\text{C}$

In order to determine location of the neutral axis, it is first necessary to determine the change in elastic strain measured by the sensor. Total strain change measured by sensor is the sum of strain changes of each strain component, as given per Equation 7:

$$\Delta \varepsilon_{tot} = \Delta \varepsilon_E + \Delta \varepsilon_T + \Delta \varepsilon_R = \Delta \varepsilon_E + \alpha_T \Delta T + \Delta \varepsilon_R \quad (7)$$

where the symbols in the equations are the following:

Symbol	Description
$\Delta \varepsilon_{tot}$	Change in total strain [ $\mu\varepsilon$ ] measured by sensor, after thermal compensation (Eq. 6)
$\Delta \varepsilon_E$	Change in elastic strain [ $\mu\varepsilon$ ]
$\Delta \varepsilon_T$	Change in thermal strain [ $\mu\varepsilon$ ]
$\Delta \varepsilon_R$	Change in rheological strain (creep and shrinkage) [ $\mu\varepsilon$ ]
$\alpha_T$	Thermal expansion coefficient of monitored material [ $\mu\varepsilon/^\circ\text{C}$ ]

As mentioned above, short-time dynamic measurements (e.g., due to passage of a very heavy vehicle), or very short-term static measurements (e.g., during the test of the bridge) should be used to evaluate location of neutral axis. In both cases the rheological strain can be neglected as the involved time period is short and insufficient to for rheological strain to develop. Thus, Equation 7, for short-time dynamic and short-term static measurements the expression for elastic strain change is given by Equation 8 (obtained by combining Equations 5, 6 and 7):

$$\Delta \varepsilon_E = \Delta \varepsilon_{tot} - \alpha_T \Delta T = \frac{1}{C_\varepsilon} \Delta \lambda_\varepsilon - \frac{1}{C_T} \left( \frac{C_{T,\varepsilon}}{C_\varepsilon} + \alpha_T \right) \Delta \lambda_T \quad (8)$$

The uncertainty of measurement of the SHM system can now be calculated applying to Equation 8 the propagation formulae given in Equation 3 or Equation 4.

Moreover, for short-time dynamic measurements, that involve time period of typically less

than one minute, temperature change will be very small. It has can be proven that for temperature change less than  $0.1^\circ$ , influence of temperature can be neglected, and the second term of right-hand side of Equation 8 can be omitted [4].

(ii) Uncertainty (error) due to the magnitude of the measured strain

Uniaxial bending is predominant in bridge structures under traffic load. In uniaxial bending the neutral axis is independent of the vertical axis, i.e., it is horizontal. For that reason, a simple and affordable SHM system with only few sensors (minimum two) per cross-section, can be used evaluate location of the neutral axis, as shown in Figure 9.

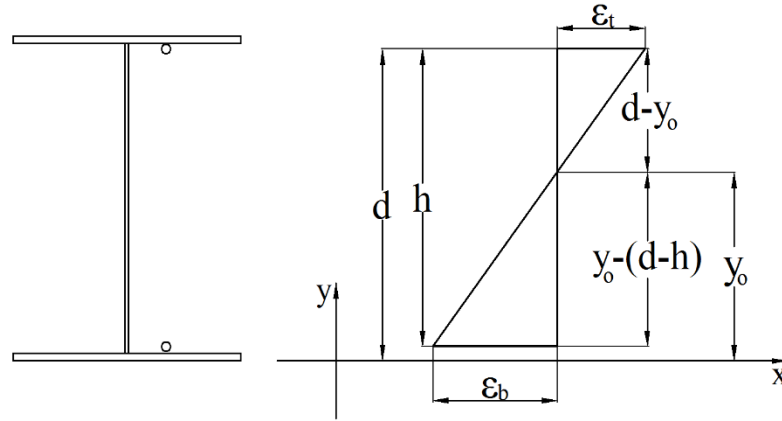


Figure 9: Left: example of cross-section equipped with two sensors for evaluation of the location of the neutral axis; Right: strain diagram in cross-section due to bending; labeling:  $\epsilon_t$  and  $\epsilon_b$  elastic strain values at the top and bottom sensor,  $h$  – distance between sensors,  $y_0$  – location of the neutral axis; and  $d$  – distance from top sensor to the bottom of the cross-section [8].

The neutral axis is parallel to the horizontal principal axis of the cross-section, and it intersects the  $y$ -axis at  $y_0$ , i.e., at location of zero elastic strain. Thus, the location of the neutral axis is given by the following equation:

$$y_0 = \frac{\epsilon_b h}{\epsilon_b - \epsilon_t} + d - h \quad (9)$$

The uncertainty in evaluation of the location of the neutral axis due to uncertainty of the elastic strain measurements can be found by applying the propagation formulae given in Equations 3 or 4 to Equation 9. For example, by applying Equation 3, the uncertainty is evaluated as follows:

$$\delta y_0 = \frac{h}{(\epsilon_b - \epsilon_t)^2} [\epsilon_b \delta \epsilon_t + \epsilon_t \delta \epsilon_b] = \frac{1 + |c|}{(1 - c)^2} \frac{1}{\epsilon_b} h \delta \epsilon \quad (10)$$

where  $\delta y_0$ , is uncertainty in location of the neutral axis and  $c = \epsilon_t / \epsilon_b$  is ratio between strain at the top of the cross-section and the bottom of the cross-section and  $\delta \epsilon$  is uncertainty in elastic strain measurement.

The influence of the magnitude of the elastic strain measurement to the uncertainty of

evaluation of location of the neutral axis is schematically shown in Figure 10.

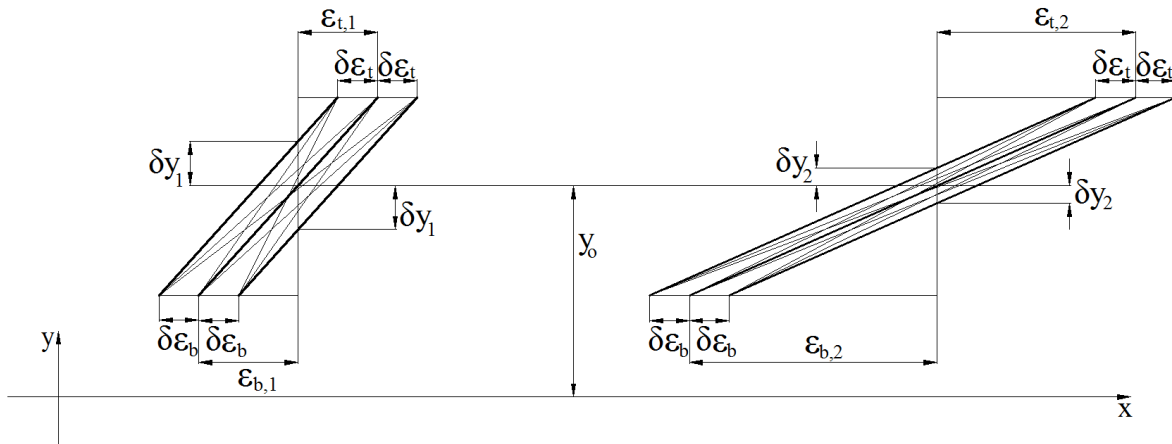


Figure 10: Schematic representation of the influence of the elastic strain magnitude to the uncertainty of evaluation of the location of the neutral axis [8].

The figure shows that larger magnitude of measured strain (left figure) implies lower uncertainty ( $\delta y_2 < \delta y_1$ ), i.e., better accuracy. This is actually numerically described by Equation 10. To relationship between the uncertainty and strain magnitude is presented in normalized diagrams in Figure 11.

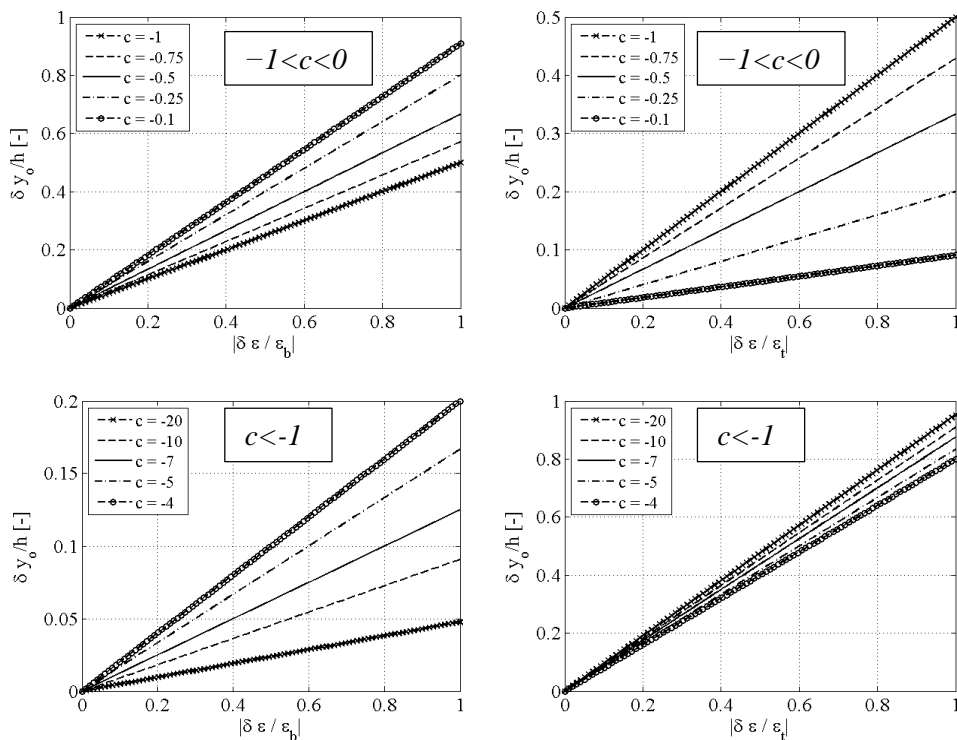


Figure 11: Normalized uncertainty in neutral axis location as a function of  $|\delta \epsilon / \epsilon_b|$  (left) and  $|\delta \epsilon / \epsilon_t|$  (right) for different values of  $c$  [8].

Figure 11 shows linear dependence, thus larger magnitude of the monitored strain, inversely proportionally smaller is uncertainty.

(iii) Uncertainty (error) due to number and position of sensors

A minimum of two sensors are needed per cross-section in order to determine the location of the neutral axis, as shown in Figure 9. If only two sensors are used, then the expression for determining the location of neutral axis is given in by Equation 9, where  $d$  and  $h$  are parameters that define the positions of sensors. The uncertainty in location of the neutral axis due to uncertainties in positions of the sensors  $\delta d$  and  $\delta h$  is then obtained by combining the propagation formulae given in Equations 3 or 4 with the Equation 9.

However, in some cases there may be more than two sensors installed per cross-section that can be used for evaluation of the location of the neutral axis. In that case, the best fit line for strain distribution across the cross-section should be found first. In general, this may be made by using simple least-square method, but this would not account for uncertainties presented in previous subsections (due to magnitude in elastic strain and positions of sensors). In order to account for all these uncertainties, other techniques are needed, and the algorithm researched by [11] is used. This algorithm is based on least-squares and maximum-likelihood analysis, and it assumes that the uncertainty in each variable (strain or location of sensors) follows a normal distribution. The best fit line is expressed as  $y=ax+b$ , and the algorithm evaluates the coefficients  $a$  and  $b$  through iteration of Equations 11-14:

$$a = \bar{Y} - b\bar{X} \quad (11)$$

where  $\bar{X} = \frac{\sum W_i X_i}{\sum W_i}$ ,  $\bar{Y} = \frac{\sum W_i Y_i}{\sum W_i}$ ,  $X_i$  is the observed strain,  $Y_i$  is the location of the sensors,

and  $W_i$  is a function of the weights on the observed strain and sensors locations.

$$b = \frac{\sum W_i \beta_i V_i}{\sum W_i \beta_i U_i}, \quad (12)$$

where  $U_i = X_i - \bar{X}$ ,  $V_i = Y_i - \bar{Y}$ , and  $\beta_i$  is a function of the weights on  $X_i$ ,  $Y_i$ ,  $U_i$  and  $V_i$ .

$$\sigma_a^2 = \frac{1}{\sum W_i} + \bar{x}^2 \sigma_b^2, \quad (13)$$

where  $\bar{x} = \frac{\sum W_i x_i}{\sum W_i}$  and  $x_i, y_i$  are the least-square-adjusted points, expectation values of  $X_i$  and  $Y_i$ .

$$\sigma_b^2 = \frac{1}{\sum W_i u_i}, \quad (14)$$

where  $u_i = x_i - \bar{x}$ .

The above algorithm evaluates the intercept of the strain distribution and its uncertainty, i.e., the neutral axis location and its uncertainty.

(iv) Uncertainty (error) due to bi-axial bending

The previous sections discussed a beam-like structure in which only uniaxial bending is expected. In real-life settings, the structure can experience biaxial bending, and an error in the evaluation of the location of the neutral axis may be introduced depending on the location of the sensors with respect to the principal axes of the cross-section. This case is schematically represented in Figure 12.

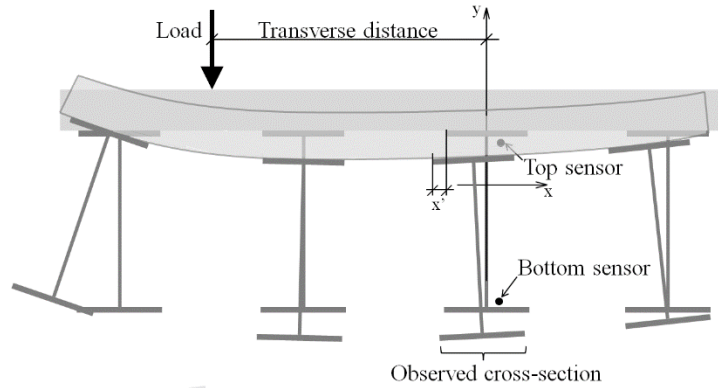


Figure 12: Schematic representation of a multi-girder bridge with a concrete slab showing biaxial bending due to transverse location of the load with respect to the observed cross-section [8].

If two or more parallel strain sensors are available, they are placed in the same vertical plane which is not located on the minor axis of the cross-section (see example for two sensors in Figure 12) the location of the neutral axis can be inaccurately determined due to bi-axial bending. Figure 13 shows that a cross-section under bi-axial bending actually has a sloped neutral axis causing the two parallel sensors to locate the neutral axis too high (or low depending on the orientation of the sensors and applied bending).

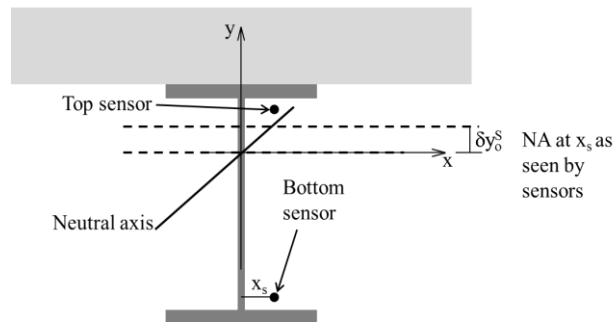


Figure 13: Schematic representation of the error in measurements using a parallel topology with two sensors under bi-axial bending (to simplify the presentation, the case presented in the figure assumes no normal force) [8].

In order to simplify the analysis, the origin of the coordinate system is located at the centroid

of the cross-section, and the position of the neutral axis at the minor principal axis is denoted with  $y_o^C$ , where the  $C$  stands for centroid. The equation of neutral axis  $y$ , under bi-axial bending and normal force is given in Equation 15.

$$\sigma(x, y) = \frac{N}{A} + \frac{M_x}{I_x} y - \frac{M_y}{I_y} x = 0 \Rightarrow y_o^C(x) = \left( -\frac{N}{A} + \frac{M_y}{I_y} x \right) \frac{I_x}{M_x} \quad (15)$$

where  $\sigma(x, y)$  is the stress within the cross-section,  $M_x$  and  $M_y$  are bending moments about the major and minor axis respectively,  $I_x$  and  $I_y$  are the moments of inertia about the major and minor axis respectively, and  $x$  and  $y$  are coordinates of points as per Figure 13. Equation 15 shows the dependence of the neutral axis on the distance from the minor axis  $x$ .

In the absence of normal force ( $N=0$ ), Equation 15 transforms to:

$$y_o^C(x) = \frac{M_y}{M_x} \frac{I_x}{I_y} x. \quad (16)$$

For sensor installed at location  $x=x_s$ , the uncertainty in the estimation of the neutral axis location given as:

$$\delta y_o^S = \frac{M_y}{M_x} \frac{I_x}{I_y} x_s. \quad (17)$$

Dependence of normalized uncertainty  $\delta y_o^S/x_s$  from the ratio  $M_y/M_x$  for different ratios of  $I_x/I_y$  is shown in Figure 14. The figure assumes that the  $x$ -axis and the  $y$ -axis are the major and minor axis respectively, and consequently,  $I_x > I_y$  and  $M_x > M_y$ .

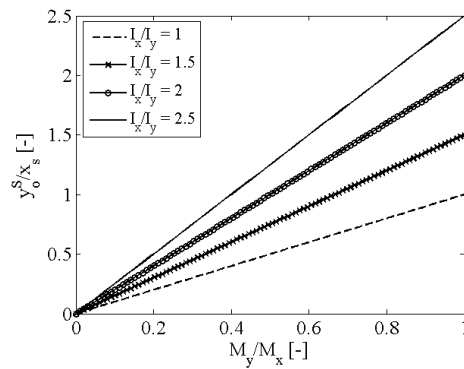


Figure 14:  $\delta y_o^S/x_s$  as a function of the ratio  $M_y/M_x$  for different ratios of  $I_x/I_y$  [8].

The figure shows that the uncertainty due to bi-axial bending can be significant. This uncertainty can be minimized by installing at least three non-coplanar sensors in the cross-section (at least three sensors that do not belong to the same vertical plane). This requirement,

however, increases the cost of the monitoring system, and the trade-off between the cost and improvement of accuracy should be well evaluated prior to installation of the sensors.

(v) Uncertainty (error) due to gauge length of sensors

The value of a measurement carried out using long-gauge strain sensor represents an average strain value along the sensor's gauge length, which is illustrated in Figure 15 and described by Equation 18.

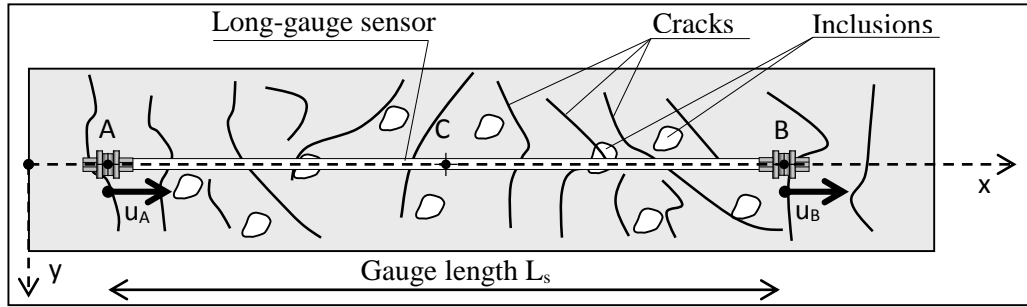


Figure 15. Schematic representation of long-gauge sensor in an inhomogeneous material [12].

$$\varepsilon_{C,s} = \frac{\Delta L_s}{L_s} = \frac{u_B - u_A}{x_B - x_A} = \frac{1}{L_s} \int_{x_A}^{x_B} \varepsilon_{x,s}(x) dx + \frac{1}{L_s} \sum_i \Delta w_{d,i} \quad (18)$$

where:  $A$  and  $B$  are points defining the gauge length of the sensor with coordinates  $x_A$  and  $x_B$ ;  $C$  is midpoint of the sensor with coordinate  $x_C = (x_A + x_B)/2$ ;  $L_s = x_B - x_A$  is the gauge length at reference time, before the deformation is applied;  $u_A$  and  $u_B$  are  $x$ -axis component of displacements of points  $A$  and  $B$  after deformation is applied;  $\varepsilon_{C,s}$  – average strain in point  $C$  measured by sensor;  $\varepsilon_{x,s}(x)$  – strain distribution along the  $x$ -axis of the sensor;  $\Delta w_{d,i}$  – dimensional change of  $i$ -th ( $x_i \in [x_A, x_B]$ ) discontinuity (crack opening, inclusion dimensional change, etc.) in direction of  $x$ -axis, after the deformation is applied.

Terms at the right side of Equation 18 show that the measured strain  $\varepsilon_{C,s}$  depends on the strain distribution  $\varepsilon_x(x)$  between points  $A$  and  $B$ , and the number and the dimensional changes of discontinuities  $\Delta w_{d,i}$  (size of crack openings or dimensional changes of inclusions) between points  $A$  and  $B$ .

In the case of non-linear strain distribution between  $A$  and  $B$ , the first term on the right side of Equation 18 is different from the real value of strain at midpoint  $C$ , and this difference in general increases as the sensor's gauge length increases. The analysis performed in [12] shows that for typical strain distributions, the following relative errors  $\delta^* \varepsilon_{C,s}$  are introduced in the strain measurement:

$$\text{Linear distribution: } \delta^* \varepsilon_{C,s} = 0; \quad (19a)$$

$$\text{Parabolic distribution: } \delta^* \varepsilon_{C,s} = -\frac{1}{3} \frac{L_s^2}{L_{Beam}^2}, \text{ where } L_{Beam} \text{ is the length of the beam; } \quad (19b)$$

$$\text{Bi-linear distribution: } \delta^* \varepsilon_{C,s} = -\frac{1}{2} \frac{L_s}{L_{Beam}}. \quad (19c)$$

The second term at the right side of Equation 18 exists only if the sensor is installed on inhomogeneous material, typically concrete. The biggest influence to the accuracy of the measurement is generated by usual cracking in reinforced concrete. In that case the error is estimated as follows [12]:

$$\delta^* \varepsilon_{C,s} \approx \pm \frac{w_c}{\Delta L_c + w_c} \cdot \frac{L_c}{L_s} < \pm \frac{L_c}{L_s} \quad (20)$$

where  $w_c$  is crack opening and  $L_c$  is distance between the cracks (typically less than 20 cm).

The final uncertainty due to gauge length of the sensor is obtained by combining propagation formulae given in Equations 3 and 4 with those given in Equations 19 and 20. It is important to notice that Equation 19 shows that shorter sensor gives better accuracy for non-linear distribution of strain, but longer sensors give better accuracy for inhomogeneous material (cracked reinforced concrete). Thus, the gauge length of sensors has to be determined as a compromise between two requirements.

### **Creation of algorithms for determination of uncertainty in deformed shape**

The accuracy in determination of deformed shape depends on [3]:

- (i) uncertainty of measurement,
- (ii) the gauge length of the sensors,
- (iii) the number and position of the sensors,
- (iv) loading pattern, and
- (v) the double integration method.

Evaluation of uncertainties related to the above points (i), (ii) and (iii) are similar to the evaluations presented previously for the neutral axis, and therefore, they are not repeated in this section.

#### Background

Assuming linear behavior of the structure, including the validity of Bernoulli's hypothesis, vertical curvature in a cross-section,  $\kappa$ , is determined from two strain measurements, as follows:

$$\kappa = \frac{\varepsilon_b - \varepsilon_t}{h} \quad (21)$$

where  $\varepsilon_b$  and  $\varepsilon_t$  are the strain values at the bottom and top of the cross-section, and  $h$  is the distance between the sensors (see Figure 9). In a beam with constant bending stiffness  $EI$ , the curvature is proportional to the moment,  $M(x)$ :

$$\kappa(x) = \frac{M(x)}{EI} \quad (22)$$

where  $E$  is Young's modulus and  $I$  is moment of inertia.

The curvature is equal to the second derivative of the deformed shape, and thus the later can be evaluated by double integration of the former, as expressed in Equation 23:

$$\kappa(x) = -\frac{d^2v(x)}{dx^2} \Rightarrow v(x) = -\iint \kappa(x) dx dx + C_1x + C_0 \quad (23)$$

where  $C_1$  and  $C_0$  are constants of integration dependent of boundary conditions.

Displacement of a beam depends on deformed shape and rigid body movement. Difference between deformed shape and displacement is shown in Figure 16. Strain sensors measure internal state of the structure, and consequently they can evaluate only the deformation, and not the rigid body movement. Thus, for deformed shape, we can adopt the boundary conditions  $v(0)=0$  and  $v(l)=0$ , where  $l$  is the length of the beam.

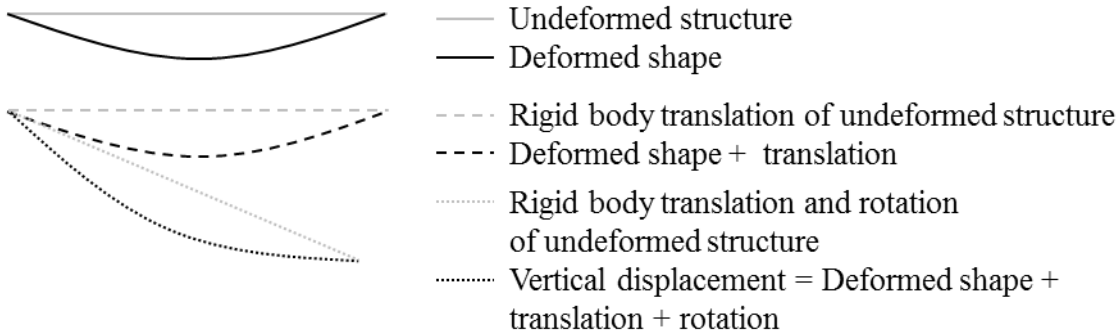


Figure 16. Deformed shape, rigid body movements, and vertical displacement [8].

If the expression for distribution of curvature along the beam is known, then the deformed shape can be determined analytically by double integration of Equation (23). However, in real structures, analytical expression for curvature is not known, and the double integration has to be performed using numerical integration methods. The two simplest and most frequently used methods are rectangle rule and the trapezoid rule. These two methods are used in this research.

Suppose the monitoring system measures the curvature,  $\kappa$ , according to Equation 21 at  $n+1$  points along a beam with length  $l$ , i.e., in points denoted with  $0, 1, \dots, n$ , as shown in Figure 17.

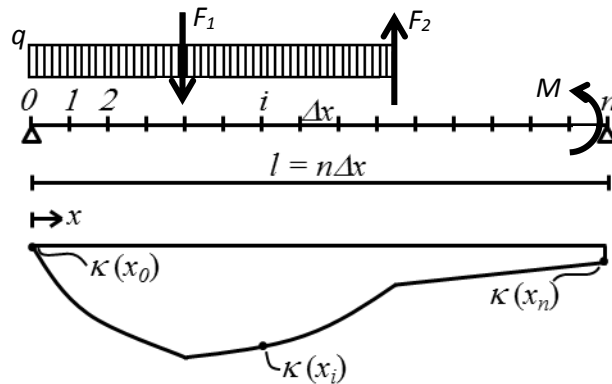


Figure 17: Curvature distribution due to concentrated forces  $F_1$  and  $F_2$ , uniform load  $q$ , and concentrated couple  $M$ , on a beam equipped with parallel sensors at  $n+1$  points [8].

To simplify the implementation of the methods, the sensor positions are made equidistant, i.e.,  $\Delta x = l/n$  is the distance between the sensor locations (see Figure 17). Then, the deformed shape  $v_R$  at sensor location  $x_i, \forall i \in \{0,1,2,\dots,n\}$ , determined by using the rectangle rule, is given by Equation 24.

$$v_R(x_i) = -\frac{l^2}{n^2} \sum_{j=1}^i \kappa(x_{j-1})(i-j+1) + \frac{il^2}{n^3} \sum_{j=1}^n \kappa(x_{j-1})(n-j+1) \quad (24)$$

The deformed shape determined by the trapezoid rule,  $v_T$ , at sensor location  $x_i$  is given by Equation 25:

$$v_T(x_i) = -\frac{l^2}{n^2} \sum_{j=1}^i \kappa(x_{j-1})(i-j+1) + \frac{il^2}{n^3} \sum_{j=1}^n \kappa(x_{j-1})(n-j+1) - \frac{l^2}{4n^2} (\kappa(x_i) - \frac{i}{n} \kappa(x_n) - (1 - \frac{i}{n}) \kappa(x_0)). \quad (25)$$

The two integration methods described by Equations (24) and (25) are independent from the load case. However, analysis of possible load cases could be useful to evaluate the uncertainty in double integration. Typical curvature distributions in real structures are combinations of linear (constant slope), bi-linear with change in slope (“broken line”), and parabolic curvature, as shown in Figure 18. Linear distribution of curvature (Figure 18A) is consequence of two concentrated moments applied at the ends of the beam. A “broken line” distribution is consequence of a concentrated force (see Figure 18B). Parabolic distribution is caused by uniformly distributed load (see Figure 18C).

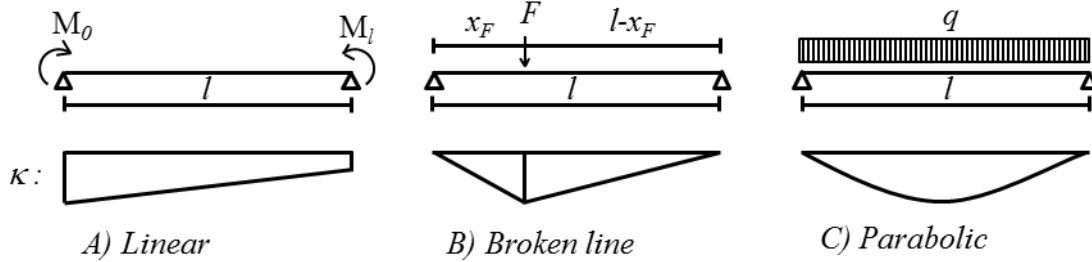


Figure 18. The three most common curvature distributions – linear, constant slope, and “broken line” – and corresponding load cases [8].

The uncertainties associated with these three load patterns are evaluated along the uncertainties of double integration in the next subsection.

#### (iv) and (v) Uncertainty (error) due to loading pattern and double integration

The accuracy of the double integration methods depends on the load pattern and the locations of the sensors. The error due to the numerical double integration is obtained for each load pattern by subtracting the analytical solution from the beam theory from the evaluations obtained from Equations 24 and 25. For each load pattern, the error term has the following form:

$$\delta v = C \kappa \frac{l^2}{n^2} \quad (26)$$

where  $C$  is a constant that depends on the load pattern and numerical integration method.

Table 1 summarize the error terms using the rectangle rule and trapezoid rule for typical load patterns shown in Figure 18.

Table 1. Error terms for rectangle and trapezoid rule for typical curvature distributions.

Curvature	Integration method	
	Rectangle rule	Trapezoid rule
Linear	$\delta v_R = 0$	$\delta v_T = 0$
Broken line, force on sensors	$\delta v_R(x_i) = \frac{4}{24} \kappa(x_i) \frac{l^2}{n^2}$	$\delta v_T(x_i) = -\frac{2}{24} \kappa(x_i) \frac{l^2}{n^2}$
Broken line, force between sensors	$\delta v_R(x_i) = \frac{1}{24} \kappa(x_i) \frac{l^2}{n^2}$	$\delta v_T(x_i) = -\frac{5}{24} \kappa(x_i) \frac{l^2}{n^2}$
Parabolic	$\delta v_R(x_i) = \frac{2}{24} \kappa(x_i) \frac{l^2}{n^2}$	$\delta v_T(x_i) = -\frac{4}{24} \kappa(x_i) \frac{l^2}{n^2}$

As an example, Figure 19 shows the error terms as a function of the number of sensor locations,  $n$ , for beam length of  $10\text{ m}$ . Typical criteria for allowed deformation in beams ( $l/250$  and  $l/500$ ) are also indicated in the figure, to help assess the number of sensors needed to evaluate these criteria.

Figure 19 shows that the trapezoid rule systematically underestimates the deformation and rectangle rule systematically overestimates it (when compared to linear analytical solution). The two approaches can therefore be considered as a lower and upper bound of the deformed shape. Hence, Table 1 and Figure 19 can actually be used at the design stage of the SHM system to determine the required number and locations of sensor along the beam needed to meet the desired accuracy in determination of deformed shape.

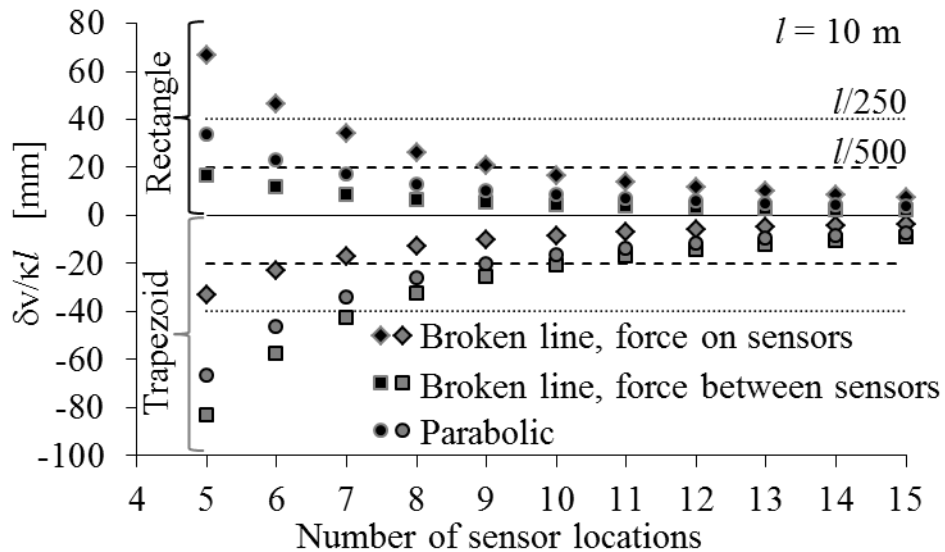


Figure 19. The error terms for double integration by the rectangle rule and trapezoid rule [8].

### Laboratory testing

The goals of previous two tasks were to determine uncertainties involved in determination of neutral axis and deformed shape, with the final aim of this project to create algorithms for evaluation and determination of the uncertainties of these two parameters, as evaluated from series of parallel long-gauge strain sensors. The performance of algorithms is validated in laboratory settings and it is presented in this section.

### Neutral axis

In order to provide a rigorous evaluation of the neutral axis location by directly including the uncertainty analysis, a weighted mean,  $\mu_w$ , is used. The reciprocals of the squared values of uncertainties determined in previous section are used as the weights in calculating the mean:

$$\mu_w = \frac{\sum_{i=1}^n \frac{y_{o,i}}{\delta y_{o,i}^2}}{\sum_{i=1}^n \frac{1}{\delta y_{o,i}^2}} \quad (27)$$

The uncertainty in the estimate of the neutral axis location,  $\mu_w$ , is then calculated as the weighted average variance of the data,  $\sigma_w^2$ :

$$\sigma_w^2 = \left( \frac{\sum_{i=1}^n \frac{y_{o,i}^2}{\delta y_{o,i}^2}}{\sum_{i=1}^n \frac{1}{\delta y_{o,i}^2}} - \mu_w^2 \right) \frac{N}{N-1} \quad (28)$$

where  $N$  represents the number of non-zero weights.

Laboratory evaluation has been performed on the large scale specimen described in Numerical Modelling section. In addition, it is important to note that the specimen had two points of artificially induced damage – a delamination was simulated above Girder A by embedding a horizontal plastic sheet of Letter Size during the pouring of concrete, and crack was simulated by embedding vertical plastic sheet above Girder K. The middle girder, Girder F was intact. Schematic of simulated damage location is given in Figure 20.

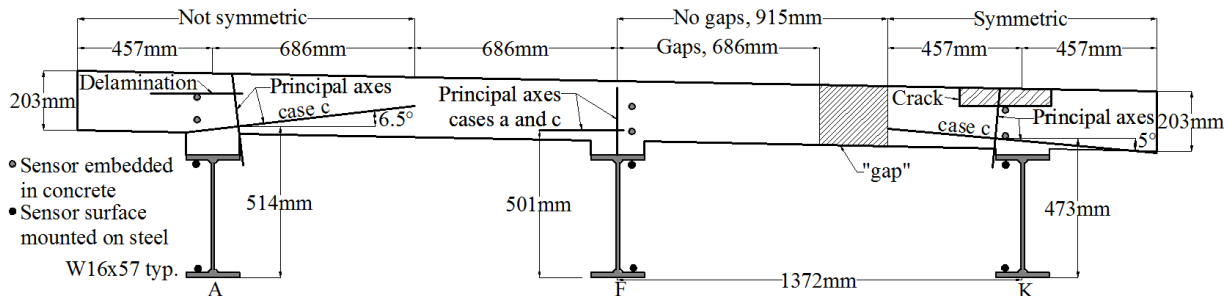


Figure 20: Schematic representation of large scale specimen and locations of simulated damage [13].

Validation is performed in two steps. First, simplified approach is taken by individually analyzing the composite girders taking into account the steel girders and contributing areas of concrete (see Figure 20). Then, more detailed analysis was performed using numerical modelling.

For simplified approach, first the location of the centroid was evaluated from geometric and material properties of the cross-section of the specimen, and then it was compared with location of the neutral axis determined from various tests. The contribution to the uncertainty in the centroid location from each of these properties was quantified. The results from this analysis for one cross-section are shown in Figure 21.

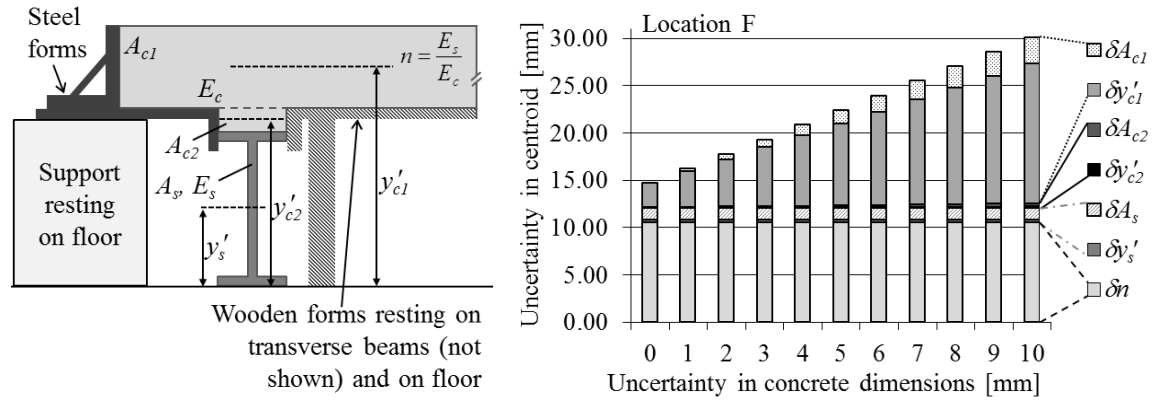


Figure 21. Schematic representation of the cross-sectional parameters needed for evaluation of the location of the centroid (left); the contributions of various parameters to the uncertainty of the location of the centroid,  $\delta y_{centroid}$  (right) [13].

The comparison between the centroid and the neutral axis location was performed using Z-score test. Figure 22 demonstrates the concept, where  $y_{centroid}$  is the location of the centroid determined from material and geometrical properties and  $\mu_w$  is the location of the neutral axis determined from measurements.

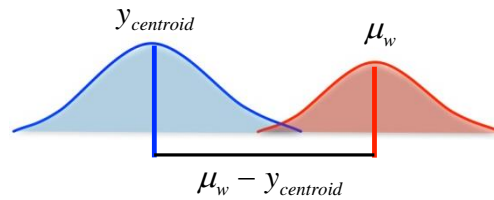


Figure 22. The centroid of the cross-section,  $y_{centroid}$ , and the neutral axis location determined from measurements,  $\mu_w$ , along with their associated uncertainties are compared with a Z-score hypothesis test [13].

The hypothesis is that the difference between  $y_{centroid}$  and  $\mu_w$  is zero, i.e. the centroid and neutral axis location are not different, and the cross-section is healthy. The Z-score is determined according to Equation 29:

$$Z = \frac{\mu_w - y_{centroid}}{\sqrt{\sigma_w^2 + \delta y_{centroid}^2}} \quad (29)$$

where  $\sigma_w^2$  is the weighted average variance of the measurements and  $\delta y_{centroid}$  is the uncertainty in the centroid determined from Figure 21.

Several events produced bending in the specimen and allowed for evaluation of the neutral axis location. These events are (i) lifting of the specimen in the factory, (ii) placing on temporary supports, (iii) second lifting, (iv) partial lifting, (v) placing on truck for transport, (vi) final placement on site. These events are shown in Figure 23.

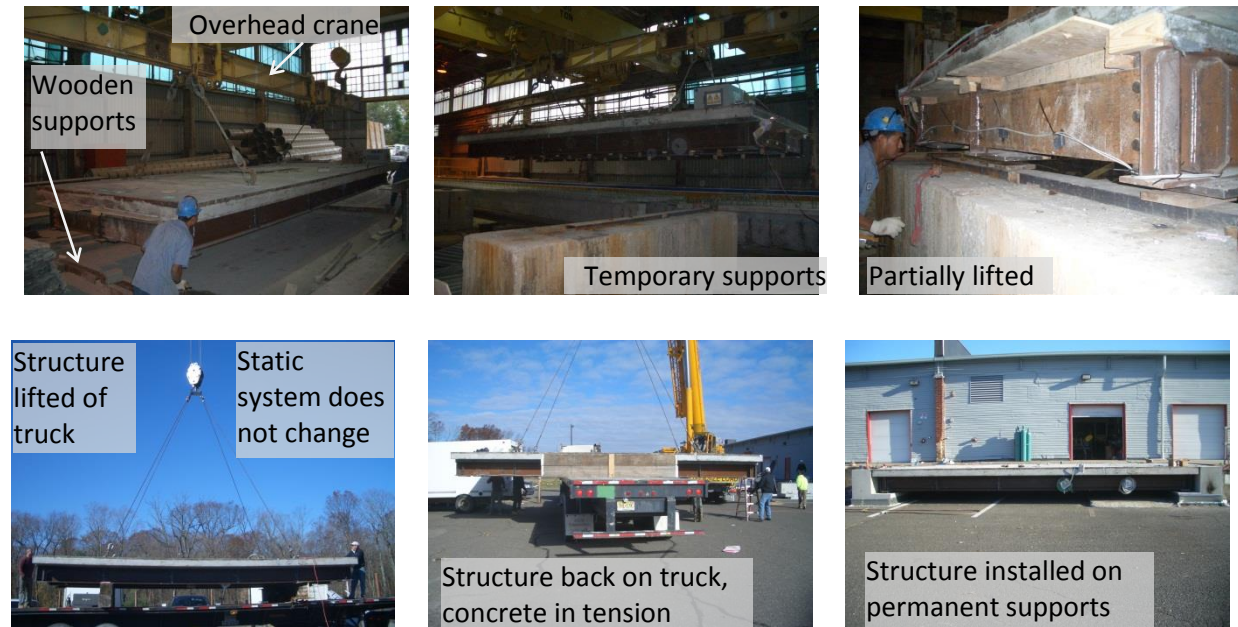


Figure 23: Various events that introduced bending in the specimen [13].

Neutral axis is compared with location of centroid in Figure 24.

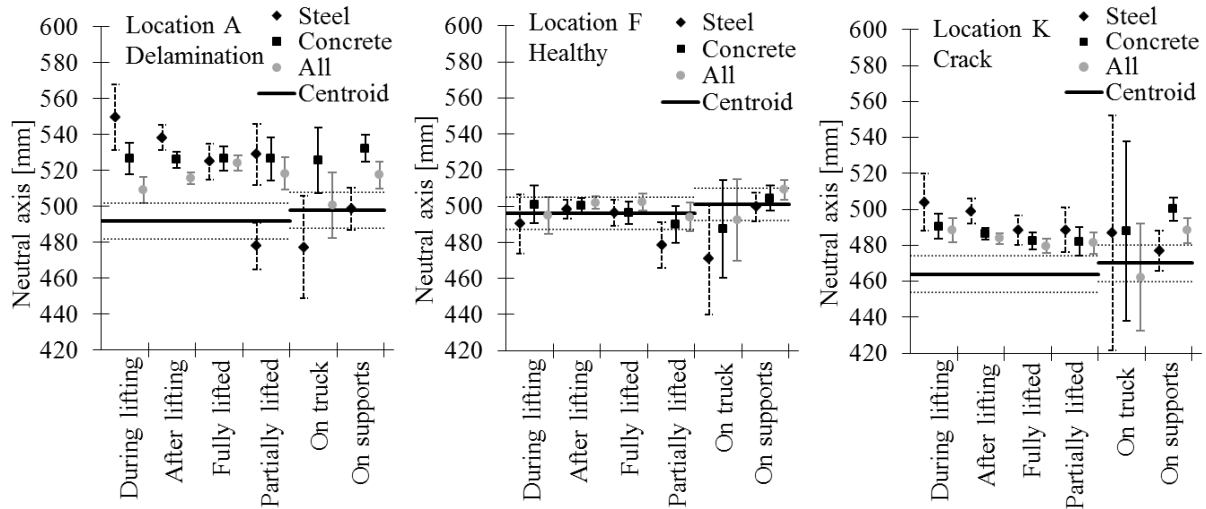


Figure 24: Comparison between the location of neutral axis and the centroid [13].

Figure 24 shows good agreement between the location of the neutral axis and the centroid at Girder F which was not damaged, but it shows discrepancies at locations of damage, indicating that damage can be detected.

Additional tests were performed in close-to-real conditions by putting the truck on the specimen (see Figure 25), and then Z-score test was performed to all available data.



Figure 25: View to truck on the large scale specimen in close-to-real conditions [13].

Results of Z-score tests are shown in Table 2. Neutral axis is determined using either only sensors installed on the steel, or on concrete, or using all sensors (see the second column of the table). The following confidence thresholds are proposed for this analysis:

≤ 10% There is highly significant difference between the centroid and the neutral axis location.

≤ 20% There is significant difference between the centroid and the neutral axis location.

Table 2: The probability that the centroid and neutral axis location are not. Bold numbers are lower than 10%, italicized numbers are between 10% and 20% [13].

		Lift 1		Lift 2		Lift 3		Tests
		During lifting	After lifting	Fully lifted	Partially lifted	On truck	On supports	
A	steel	<b>0</b>	<b>0</b>	<b>2</b>	<b>6-40</b>	48	95	12
	concrete	<b>1</b>	<b>1</b>	<b>0</b>	<b>3</b>	17	<b>0</b>	<b>0</b>
	all	16	2	<b>0</b>	<b>5</b>	88	<b>10</b>	<b>1</b>
F	steel	74	85	100	25	35	94	72
	concrete	73	68	100	65	62	79	84
	all	94	53	56	86	70	44	70
K	steel	<b>3</b>	<b>0</b>	<b>6</b>	<i>12</i>	79	64	33
	concrete	<b>3</b>	<b>4</b>	<i>11</i>	<i>16</i>	73	<b>1</b>	<b>6</b>
	all	<b>5</b>	<b>5</b>	<i>16</i>	<i>14</i>	48	<i>14</i>	20

Table 2 is graphically represented in Figure 26. The table and figure confirm that there is a good agreement between the location of the neutral axis and centroid at healthy Girder F. This practically validates the evaluation of uncertainties, which was the aim of this section.

In addition, the damaged Girders A and K have a higher likelihood that the neutral axis and centroid are not the same. For Girders A and K, more than 75% of the predications show less than 20% likelihood that the neutral axis and centroid coincide, which practically indicates damage detection.

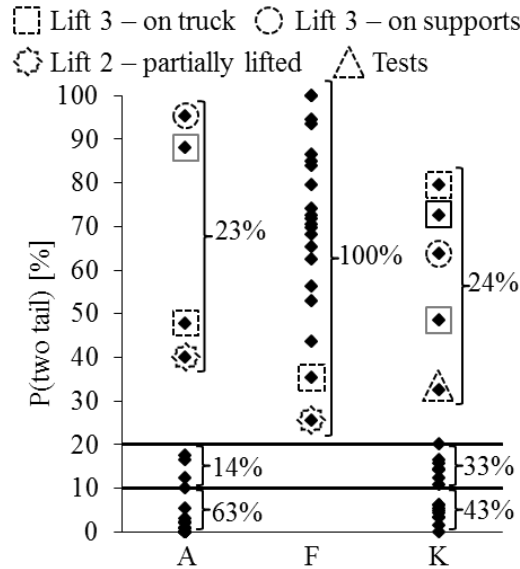


Figure 26: Results of Z-score tests - the probability that the centroid and the neutral axis location coincide for Girders A, F, and K [13].

Table 2 and Figure 26 show that the location of the neutral axis is sensitive to minute damage occurring in form of delamination and cracking in the concrete slab. However, according to linear theory of structures and the literature review, the neutral axis location at damaged location of the specimen is expected to move down, and not up as shown in Figure 24.

To better understand the behavior of the neutral axis in composite beam structures in the presence of damage, numerical modelling was used to test the sensitivity of the neutral axis movement to the damage using the finite element model of the large scale specimen (see the section on numerical modelling).

Prescribed minute damage in the large scale specimen was incorporated into the finite element model as seams inside the mesh of the concrete slab. A sensitivity analysis was performed on the neutral axis position as the width and depth of the crack in the concrete slab is varied. The neutral axis position for each damage scenario was extracted by locating the position of zero strain in the cross-section of the structure at midspan. Figure 27 summarizes a comparison of the neutral axis position from each damage scenario to that of the healthy structure.

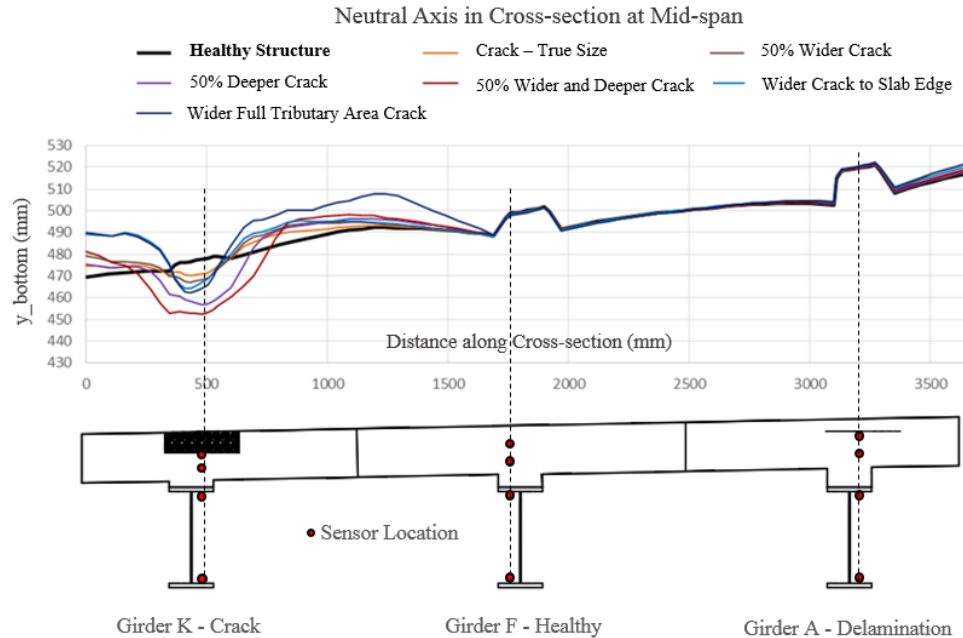


Figure 27: Neutral axis position sensitivity analysis – crack size [9].

As shown in Figure 27, the neutral axis moves to lower positions at the sensor location at Girder K, which is very close to the position of the prescribed crack. Also, damage induced within the tributary area of Girder K does not affect the neutral axis position at other girder locations, which indicates that the variation is fairly local. Furthermore, it is observed that upward movement of the neutral axis occurs inside the concrete slab on either side of the crack location, and the maximum shift of neutral axis position appears to be proportional to the size and severity of damage.

Based on this sensitivity analysis, depending on the size of the damage and the relative position of the strain sensors, both upward and downward movement of the neutral axis can be detected. This conclusion justifies the trends observed from sensor measured neutral axis positions for the large scale specimen and the US202/NJ23 overpass (see the next section).

In a subsequent sensitivity analysis, the impact on the neutral axis due to imperfect support conditions was studied. In structural design and analysis, the support conditions of structures are often assumed to be idealized. However, imperfect support conditions are likely to occur due to factors such as uncertainties and errors in the fabrication process, malfunctioning of supports, as well as differential support settlements. In typical beam-like structures, differential displacement of a few millimeters at support locations can alter reaction forces and induce noticeable strain redistribution in the overall structure. Therefore, although imperfect support condition may not be considered as direct physical damage to the bridge superstructure, locations of high support reactions are likely to induce physical damage in the structure over time.

Three damage scenarios were simulated using the finite element model of the large scale specimen where the structure is simply supported and placed under self-weight. For each of the three damage scenarios, the support reactions at one of the girder locations was removed to

create redistribution of reaction forces. The neutral axis position was extracted from the model of the damaged structure, as shown in Figure 28.

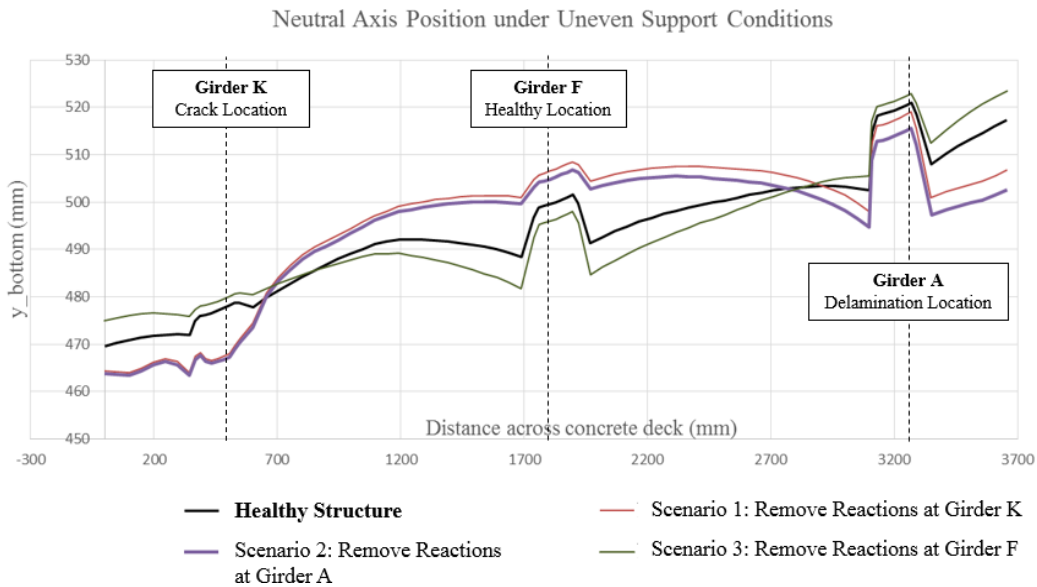


Figure 28: Neutral axis position sensitivity analysis – imperfect support condition [9].

Based on the results from Figure 28, it can be observed that for Scenarios 1 and 2, where reactions from a side support were removed, the neutral axis position moves upward near the center of the cross-section, and downwards near Girder K and Girder A. For scenario 3, when reactions from Girder F are removed, the neutral axis moved downward locally near the closest sensor location, and upward at the Girders A and K.

According to these results, imperfect support conditions can cause bi-directional movement of the neutral axis in a multi-girder beam structure, which could have contributed to the bi-modal and upward shifts of the neutral axis observed from the analysis of sensor data.

So far, the analysis of the neutral axis has been focused on comparing the measured neutral axis position at sensor locations to that of the predicted healthy neutral axis position. In this section, the effect of damage on the distribution of the neutral axis measured by different sets of sensors at a given location of interest will be studied.

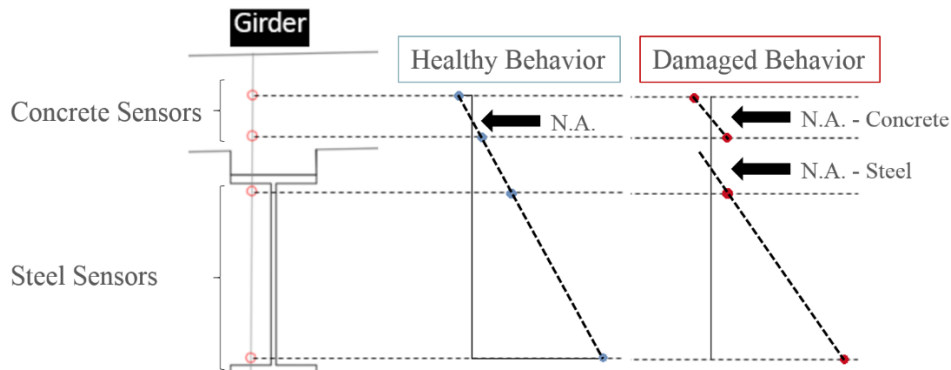


Figure 29: Dispersion of neutral axis in healthy and damage sections [9].

As shown in Figure 29, in a healthy composite section, the strain sensor readings are expected to follow a linear strain profile, and the neutral axis position would be unique. However, in the presence of damage, the section would have a non-linear strain profile, and the position of neutral axis measured depends on the sensor set used. Therefore, when sensor data is available from three or more strain sensors at each location of interest, the dispersion of the neutral axis position measured by different sensor sets can be used for damage detection.

The Z-score test, which compares the agreement of two distributions, can be calculated using the mean ( $x_i$ ) and variance ( $s_i$ ) of the neutral axis position measured by two sensor sets, as shown in Equation 30, which is practically identical with Equation 29, with changed arguments. Assuming healthy structural behavior, the neutral axis measured by the two sets of sensors shall be identical, which corresponds to a  $\Delta$  value of zero.

$$Z = \frac{(x_1 - x_2) - \Delta}{\sqrt{(s_1)^2 + (s_2)^2}} \quad (30)$$

The *P value*, which represents the probability that the neutral axis positions measured by the two sets of sensors are not different, can then be calculated based on the *Z-score*. The range of the *P value* is 0 to 100%, where a high *P value* represents the healthy linear strain behavior, and a low *P value* indicates damage in the monitored section.

This method was applied to neutral axis measurements of the large scale specimen, when the structure was placed on temporary supports. The mean and standard deviation of the neutral axis position at each girder location measured by concrete and steel sensor sets were used for the analysis, as shown in Figure 30 below. The *P value* at the reference location was calculated to be 96%, which confirms healthy behavior. At Girders A and K, where minute damage was located, the *P values* were calculated to be 5% and 2% effectively, which indicates damaged behavior.

Based on these results, the dispersion of the neutral axis is very effective for predicted minute crack and delamination in composite structures, and has great potential as a damage indication parameter.

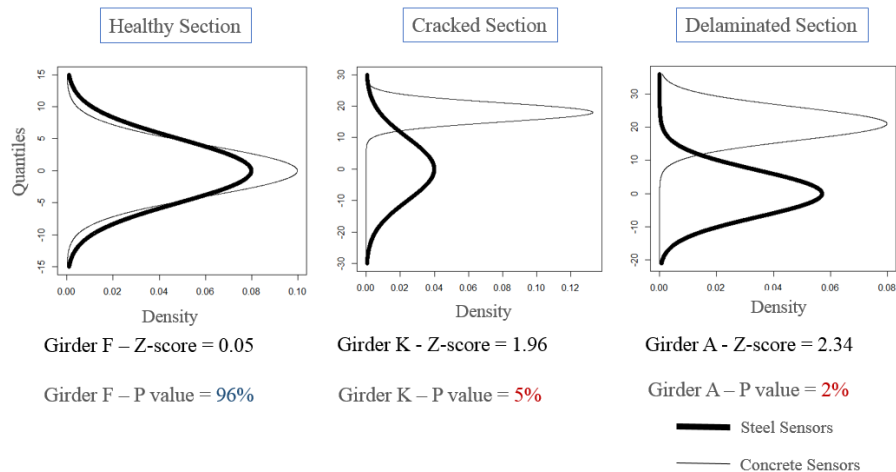


Figure 30: Dispersion of neutral axis – large scale specimen [9].

Based on these results, the dispersion of the neutral axis is very effective for predicted minute crack and delamination in composite structures, and has great potential as a damage indication parameter.

### Deformed shape

The accuracy in prediction of uncertainty deformed shape was assessed on a small scale specimen described in the section on numerical modelling. Five fiber Bragg-grating (FBG) fiber-optic strain sensors with gauge length of 10 cm were installed on the top of the specimen with equal spacing. Four LVDT displacement meters were used to measure deflection and to perform necessary transformation of deflection to deformed shape. Assuming linear behavior of the specimen, and taking into account the absence of normal force in the specimen, it was possible to calculate curvatures at each instrumented cross-section from measurements. Two configurations were tested, a cantilever and simply supported beam. Both concentrated and uniformly distributed force were applied, as shown in Figure 31.

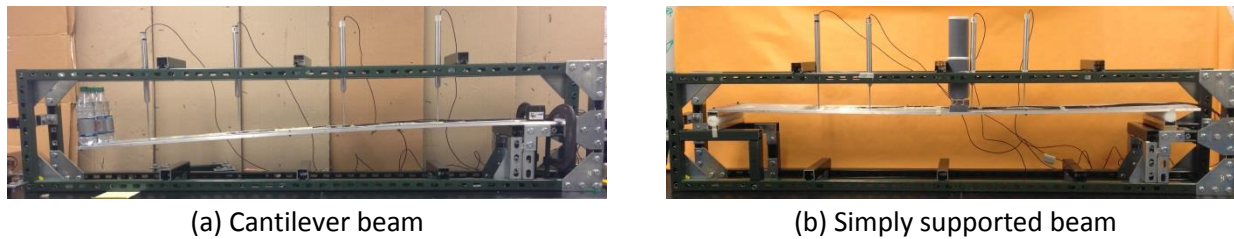


Figure 31. Small scale specimen testing setup [8].

The specimen in cantilevered-beam configuration was loaded at the free end with three loads, 1P = 5.8 N, 2P = 11.6 N, and 3P = 17.4 N. The measurements were taken with the FBG sensors and LVDT's. The measured curvatures were in good agreement with linear theory of beams, see Figure 32a. Then, Equations 24 and 25 were used to evaluate the deformed shape as shown in Figure 32b. The curvature diagram in Figure 32a is linear and therefore no error is expected from the double integration (see Table 1). The uncertainty from the mechanical strain measurement was in the order of 0.01-0.05 mm and thus practically invisible in the figure, thereby validating the procedure for evaluation of deformed shape and the associated uncertainty analysis.

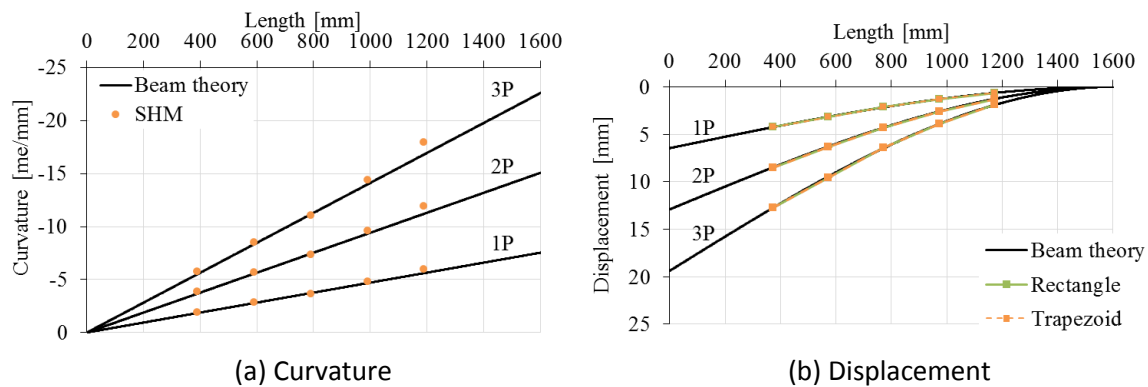


Figure 32. The curvature and deformed shape of the small scale specimen loaded in cantilevered-beam configuration [8].

The configuration of the small scale specimen was rearranged into simply supported beam, and it was loaded with  $1P = 29.9\text{ N}$ ,  $2P = 59.4\text{ N}$ , and  $3P = 89.2\text{ N}$ , close to the middle of the span. Figure 33a confirms good agreement between measured and analytically determined curvature. Excellent agreement is obtained as well between deformed shapes calculated using Equations 24 and 25, and analytical solution, i.e., thereby validating the procedure for evaluation of deformed shape and the associated uncertainty analysis.

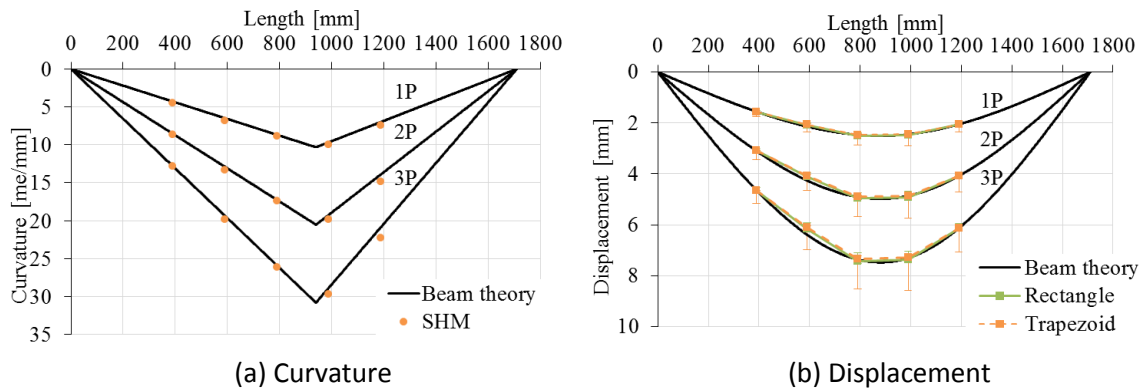


Figure 33. The curvature and deformed shape of the small scale specimen loaded approximately at the middle of the span, simple-beam configuration [8].

Several other tests were conducted on the simple-beam configuration, with different load cases, that combined concentrated forces and uniformly distributed force. The results and the load cases are presented in Figures 34 and 35.

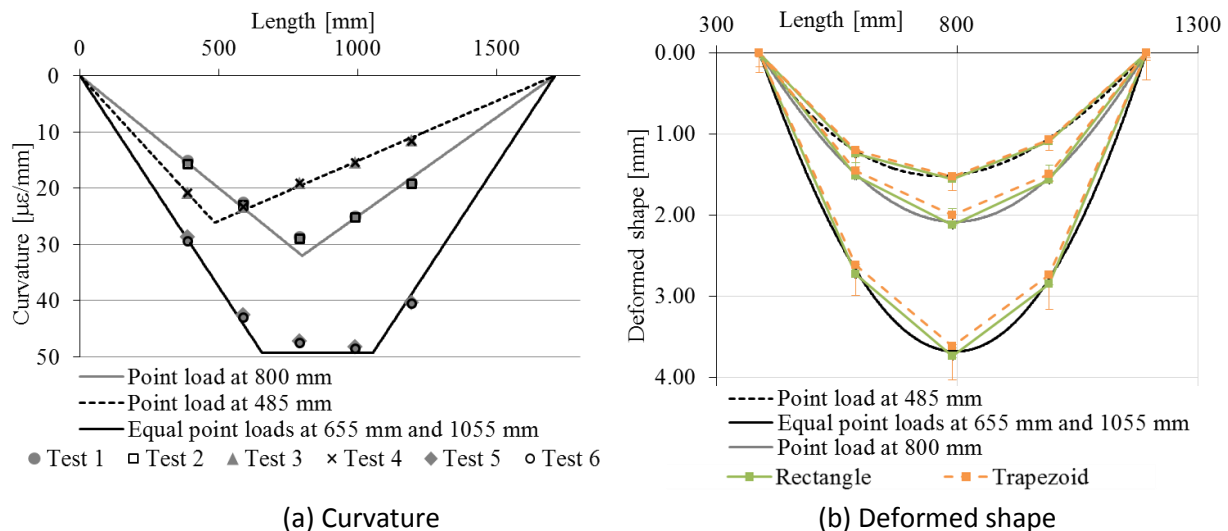
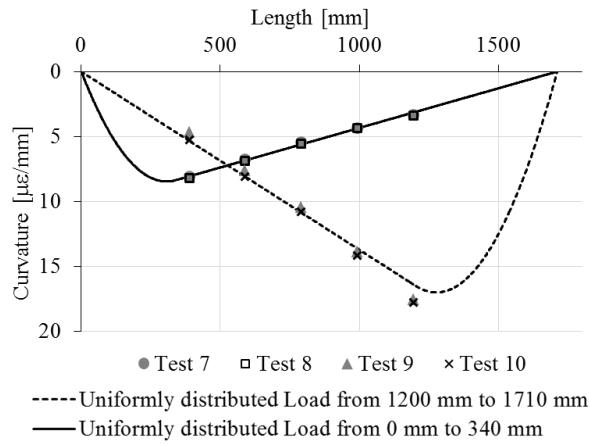
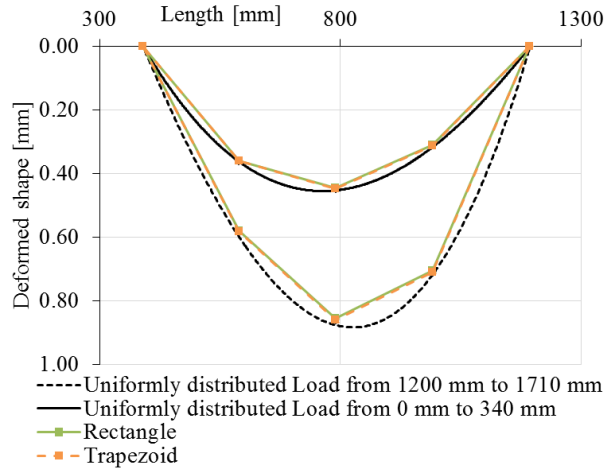


Figure 34. The curvature and deformed shape of the small scale specimen loaded with concentrated force at various locations, or with combination of forces, simple-beam configuration [8].



(a) Curvature



(b) Deformed shape

Figure 35. The curvature and deformed shape of the small scale specimen loaded with combination of concentrated force and uniformly distributed force [8].

These above examples practically validated the evaluation of deformed shape and associated uncertainties in laboratory conditions.

### On-site validation

The goals of the previous task was to validate in laboratory settings the algorithms for evaluation of uncertainties in determination of the neutral axis and deformed shape. Their validation in on-site conditions is presented in this section.

#### Neutral axis

The algorithms for determination of uncertainties in the position of the neutral axis were validated on both, the US202/NJ23 overpass and Streicker Bridge.

Figure 36 shows the mean and standard deviation of the neutral axis location at midspan of Girder 5 of the US202/NJ23 overpass for the measurement sessions performed over 4 years. The histogram presented over the cross-section (to the left) shows a typical distribution of the neutral axis location during one measurement session (session from March 2013 presented in the figure). Diagram to the right shows the uncertainties as calculated by algorithms developed in this project. An excellent agreement is obtained, which validates the algorithms.

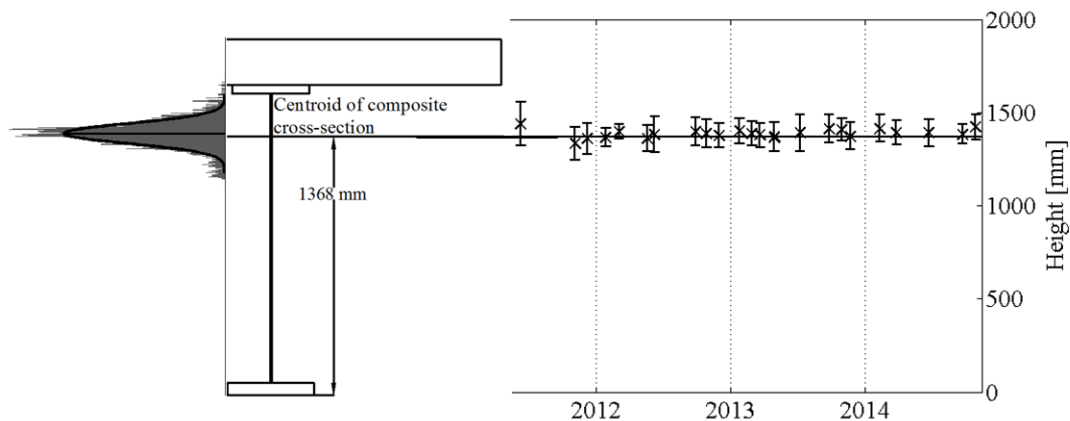


Figure 36: Evaluation of uncertainties in determination of location of the neutral axis at midspan of girder 5 of the US202/NJ23 overpass [8].

A load test was performed on the southeast leg of the Streicker Bridge in March 2011, and the collected data was used to evaluate the uncertainties in location of the neutral axis. The load was applied to the bridge by means of four golf-carts with passengers. First, the load was gradually increased by bringing the cars one by one, and then it was gradually decreased by removing the cars one by one. The neutral axis location was evaluated after each step of load. As an example, the results for location P11 are shown in Figure 37.

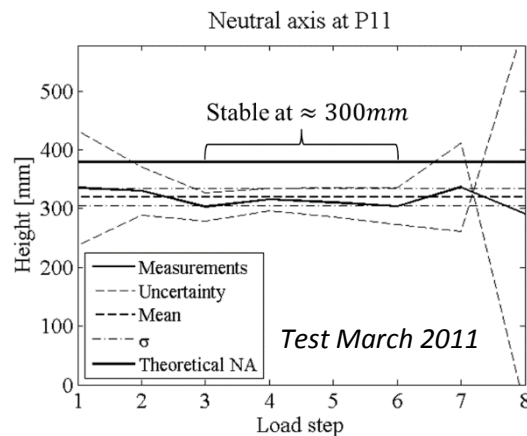


Figure 37: Evaluation of the location of the neutral axis and associated uncertainty [8].

During the first two load steps, the uncertainty is high due to low strain magnitude. Similar result is confirmed in the last two load steps. The results of the test validated the algorithms for evaluation of uncertainties.

### Deformed shape

The algorithms for determination of uncertainties in the deformed shape were validated on Streicker Bridge. In April 2014 a load test was performed using an approximately four-metric-ton truck that was positioned in the middle of the longest span of the southeast leg. Direct measurements of vertical displacement along the bridge, needed for validation of algorithms, were not available except in one point at the middle of the longest span. Therefore, the deformed shape as determined from the SHM system were compared to a Finite Element Model

(FEM) simulation of the test. The FEM was calibrated, based on known input and strain measurements. The results of the comparison are presented in Figure 38, along with the uncertainties in determination of deformed shape evaluated as per algorithms developed in this project.

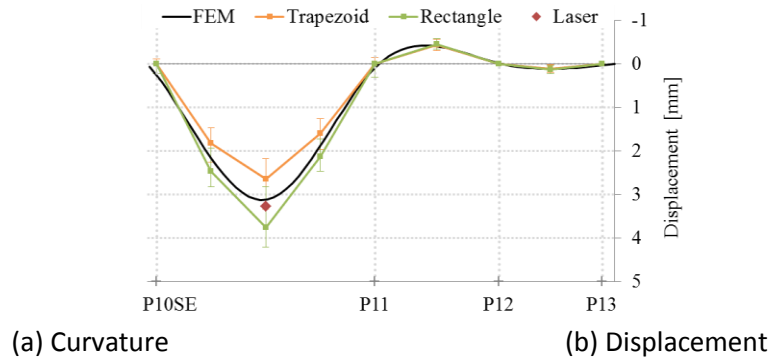


Figure 38. Deformed shape of the southeast leg of Streicker Bridge as obtained from SHM and FEM [8].

To further validate the results, an independent, laser-based displacement measurement was performed by a research group from Columbia University. The measurement, included in Figure 37, observes a similar displacement predicted by the FEM, thus confirming that it captures well the behavior of the bridge. The results of the test practically validate the algorithms for evaluation of uncertainties in deformed shape, since the FEM and deformed shape determined from SHM are always within uncertainty limits.

## CONCLUSIONS

Several major conclusions can be drawn from this project:

1. The literature review revealed a need for better understanding of uncertainties involved in determination of neutral axis and deformed shape of beam-like structures. This finding justified research carried out in this project.
2. Algorithms for evaluation of uncertainties in determination of location of the neutral axis were created and validated both in laboratory settings and real-life settings. The uncertainties associated with the following phenomena were studied:
  - Uncertainty of measurement of the SHM system,
  - The magnitude of the measured strain,
  - Number and position of sensors,
  - Bi-axial bending,
  - Gauge length of sensors,

The uncertainties associated with the following phenomena will be studied in the future:

- The change in axial strain,
- The size of SHM data sets,
- Dynamic effects,
- The position of the load on multi-girder systems.

3. Algorithms for evaluation of uncertainties in determination of deformed shape based on double integration of the curvature were created and validated both in laboratory settings and real-life settings. The uncertainties associated with the following phenomena were studied:
  - Uncertainty of measurement,
  - The gauge length of the sensors,
  - The number and position of the sensors,
  - Loading pattern,
  - The double integration method.

The determination of deformed shape based on conjugate beam method will be studied in the future.

4. Neutral axis and deformed shape are universal parameters found in every beam-like structure. Thus, the results of this project are practically applicable to large variety of structures, as follows:
  - evaluation of uncertainties is paramount in setting the thresholds for detection of unusual behaviors (detection of damage or alteration in performance)
  - possibility to predict uncertainties enables and informs quantitative design of sensor network (required density of sensors to achieve desired uncertainty)
  - the network consisting of parallel sensors is used for both determination of position of neutral axis and deformed shape, thus the same sensor network enables determination of both parameters, which makes it very efficient
  - to apply the methods, it is not necessary to know the loads on the structure or to stop the traffic, which makes both methods easy to apply,
  - neutral axis and deformed shape are well known parameters in structural engineering, and the SHM methods based on these parameters are easily understood by structural engineers.

## **PUBLICATIONS RESULTING FROM THE PROJECT**

### Theses

1. Li, X. (2016). Validation of the Method of Neutral Axis for the Identification of Minute Damage in Composite Beam Structures, M.S.E. Thesis, Princeton University, Princeton NJ.
2. Sigurdardottir, D. (2015). Strain-based monitoring methods for beam-like structures, Ph.D. Thesis, Princeton University, Princeton NJ, USA.

### Journal Papers

1. Li, X., Glisic, B. (2016/17). Evaluation of influence of minute damage to change in location of the neutral axis, *in preparation*.
2. Sigurdardottir, D.H., Stearns, J., and Glisic, B. (2016/17). Uncertainty in determination of the deformed shape of beams using strain measurements, *in preparation*.
3. Sigurdardottir, D.H., Glisic, B. (2015). The neutral axis location for structural health monitoring – an overview, *Journal of Civil Structural Health Monitoring*, 5(5):703-713.

4. Sigurdardottir, D.H., Glisic, B. (2015). On-Site Validation of Fiber-Optic Methods for Structural Health Monitoring: Streicker Bridge, Journal of Civil Structural Health Monitoring, 5(4):529-549.
5. Sigurdardottir, D.H., Glisic, B. (2014). Detecting minute damage in beam-like structures using the neutral axis location, Smart Materials and Structures, 23, art. no. 125042 (15pp).

Conference papers:

1. Li, X., Glisic, B. (2016). Finite Element Verification of the Method of Neutral Axis for Damage Detection in Composite Beam Structures, 8th European Workshop on Structural Health Monitoring, EWSHM 2016, Bilbao, Spain, July 5-8, 2016.
2. Glisic B., Sigurdardottir D.H., Abdel-Jaber H., Kliewer, K., Li X., Reilly J. (2016). Recent contributions to strain-based structural health monitoring using long-gauge fiber optic sensors – an overview, 6-CSHM – 6th Workshop on Civil Structural Health Monitoring, Belfast, UK, May 26-27, 2016 .
3. Li, X., Glisic, B. (2016). Identification of minute damage in composite bridge structures equipped with fiber optic sensors using the location of neutral axis and finite element analysis, Proceedings of SPIE Vol. 9805, 980524, 6pp.
4. Domaneschi, M., Sigurdardottir, D., Glisic, B. 2015. Challenges in damage detection based on finite element analyses and monitoring of dynamic curvature of concrete-steel composite structures, 10<sup>th</sup> International Workshop on Structural Health Monitoring – IWSHM2015, Stanford University, September 2015.
5. Abdel-Jaber, H., Sigurdardottir, D., Glisic, B. (2015). Damage Detection using Neutral Axis and Prestressing Force Distribution, Proceedings of IABSE Conference 2015, Geneva, Switzerland, September 23-25, 2015.
6. Li, X., Glisic, B., (2015). Evaluating the State of a Section under Bending Using the Location of Neutral Axis, Proceedings of 2015 IEEE Workshop on Environmental, Energy and Structural Monitoring Systems, Trento, Italy, July 9-10, 2015.
7. Cappello, C., Sigurdardottir D., Glisic, B., Zonta, D., Pozzi M. (2015). On predicting monitoring system effectiveness, Proceedings of SPIE - The International Society for Optical Engineering 9435-92 (special mention at 2015 SPIE SS/NDE conference).
8. Sigurdardottir, D., Glisic, B. (2014). Examples of damage detection in real-life settings based on the position of the neutral axis, 7th European Workshop on Structural Health Monitoring (EWSHM), Nantes, France, July 8-11, 2014, paper on conference CD.

**RECOMMENDATIONS**

This project have demonstrated that it is possible to evaluate accurately the uncertainties in determination of position of neutral axis and deformed shape of beam-like structures using a

network of parallel sensors. The following recommendations are proposed based on experience and results from the project:

1. Location of the neutral axis: minimum two parallel sensors in a cross-section should be used to evaluate the location of the neutral axis; however, in the case of composite steel-concrete structures, redundancy is recommended, and more accurate results are obtained if pair of sensors is embedded in concrete slab, and another pair of sensors is installed on steel girder; this configuration demonstrated higher sensitivity to minute damage.
2. Minimization of uncertainty in location of the neutral axis:
  - a. to minimize uncertainty related to monitoring system, a proper installation of the monitoring system is needed (good strain transfer from the structure to sensor), and repeated dynamic measurement are recommended (to minimize thermal compensation and temperature influence to the structure);
  - b. to minimize uncertainty related to strain magnitude, the sensors within a monitored cross-section should be as distant as possible from the centroid of stiffness;
  - c. to minimize uncertainty related to gauge length of sensors, the gauge length should be determined based on principles presented in literature [12];
  - d. to minimize influence of bi-axial bending, three or more non-coplanar sensors should be installed in the cross-section; however, this increase the cost;
3. Deformed shape: both trapezoid and rectangle rule should be used for double-integration of curvature – the former will provide the lower limit (by absolute value) and later the upper limit of estimation of deformed shape;
4. Minimization of uncertainty in determination of deformed shape:
  - a. parallel sensors should be placed in equidistant cross-sections along the structure; this simplifies the evaluation of uncertainties;
  - b. to minimize uncertainty related to strain magnitude, the sensors within a monitored cross-section should be as distant as possible from the centroid of stiffness;
  - c. number of cross-sections to be instrumented by sensors should be determined so that the uncertainty fall below acceptable limit;
  - d. points 3a and 3c from above apply to this point too.
5. Since the same sensor network enables monitoring of both, neutral axis and deformed shape, it is recommended to consider both parameters simultaneously when designing the sensor network.

## REFERENCES

- [1] ASCE. 2011. Failure to act, the economic impact of current investment trends in surface transportation infrastructure.
- [2] US-DOT, FHWA, FTA. 2012. 2010 Status of the Nation's Highways, Bridges and Transit: Conditions and Performance. Report to Congress.

- [3] Glisic, B. 2014. Fiber optic monitoring methods for composite steel-concrete structures based on determination of neutral axis and deformed shape, Final Report, Report No. CAIT-UTC-012, January 2014.
- [4] Kirkup, L, Frenkel, B. 2006. Introduction to Uncertainty in Measurement, Cambridge University Press.
- [5] Rabinovich, S.G. 2005. Measurement Errors and Uncertainties, Theory and Practice, 3rd Edition, Springer.
- [6] Sigurdardottir, D.H., Glisic, B. 2013. Neutral axis as damage sensitive feature, Smart Materials and Structures, 22(7), art. no. 075030 (18pp).
- [7] Domaneschi, M., Sigurdardottir, D., Glisic, B. 2015. Challenges in damage detection based on finite element analyses and monitoring of dynamic curvature of concrete-steel composite structures, 10th International Workshop on Structural Health Monitoring – IWSHM2015, Stanford University, September 2015.
- [8] Sigurdardottir, D. (2015). Strain-based monitoring methods for beam-like structures, Ph.D. Thesis, Princeton University, Princeton NJ, USA.
- [9] Li, X. (2016). Validation of the Method of Neutral Axis for the Identification of Minute Damage in Composite Beam Structures, M.S.E. Thesis, Princeton University, Princeton NJ.
- [10] Hubbell, D., Glisic, B. 2013. Detection and Characterization of Early Age Thermal Cracks in High Performance Concrete, ACI Materials Journal, 110 (3), pp. 323-330.
- [11] York, D., Evensen, N.M., Martinez, M.L., Delgado, J.D.B. 2004. Unified equations for the slope, intercept, and standard errors of the best straight line, Am. J. Phys. 72 367–75.
- [12] Glisic, B. 2011. Influence of gauge length to accuracy of long-gauge sensors employed in monitoring of prismatic beams, Measurement Science and Technology, 22 (3), art. no. 035206 (13pp).
- [13] Sigurdardottir, D.H., Glisic, B. 2014. Detecting minute damage in beam-like structures using the neutral axis location, Smart Materials and Structures, 23, art. no. 125042 (15pp).